Single-atom catalysts for electrochemical N_2 reduction to NH_3

Muhammad Saqlain Iqbal, Zhibo Yao, Yukun Ruan, Ramsha Iftikhar, Leiduan Hao*, Alex W. Robertson, Syed Muhammad Imran, Zhenyu Sun*

Muhammad Saqlain Iqbal, Syed Muhammad Imran
State Key Laboratory of Organic-Inorganic Composites, College of Chemical Engineering, Beijing University of Chemical Technology, Beijing 100029, P. R. China
Department of Chemical Engineering, COMSATS University Islamabad, Lahore campus, Defense Road, 54000-Lahore, Pakistan

Z Yao, Y Ruan, L Hao*, Z Sun*
State Key Laboratory of Organic-Inorganic Composites, College of Chemical Engineering, Beijing University of Chemical Technology, Beijing 100029, P. R. China
email: haold@buct.edu.cn; sunzy@mail.buct.edu.cn

Ramsha Iftikhar
Department of Chemistry, Government College University, Faisalabad 38000, Pakistan

Alex W. Robertson
Department of Physics, University of Warwick, Coventry CV4 7AL, U. K.

Abstract With the increasing demand for clean energy and growing concerns regarding environmental sustainability, the production of clean fuels via green chemistry is attracting greater attention. In this respect, ammonia is a green alternative to fossil fuels and could serve as a clean energy source. There is now great interest in realizing the electrochemical reduction of atmospheric nitrogen (N_2) for cheap, environmentally friendly and reliable ammonia production worldwide. However, the robustness of the triple bond in N_2 and the low efficiency of candidate catalysts limit the utility of this conversion. Single atom catalysts have been found to be more effective than nanoparticles due to their unique properties and have been employed extensively for the nitrogen reduction reaction (NRR). In this review, we have covered recent advances in the design and synthesis of noble metal and non-noble metal single atom catalysts (SACs) for the electrochemical reduction of nitrogen during the years of 2018−2022. The catalyst efficiencies,

with reference to coordination preferences and theoretical studies, have been discussed. Moreover, we also provide insights into the current challenges and some considerations for further studies.

Keywords N_2 reduction; Single atom catalyst; Electrocatalysis; NH_3

1 Introduction

Ammonia (NH_3) is an essential and commonly used basic chemical. Currently, the world produces 2.35×10^8 metric tons of it, but that number is predicted to rise to 2.9×10^8 metric tons by 2030. Furthermore, it is predicted that the worldwide ammonia market would reach US$ 76.64 billion by 2025 [1]. The vast majority of the NH_3 produced is utilized to make agricultural fertilizers. In addition, NH_3 is used to manufacture medications, synthetic fibers, explosives, plastics, rubber, and other products [2, 3]. NH_3 is a prospective H_2 energy carrier because of its high energy density (17.6% H content) and comparatively cheap transportation costs after the fast growth of renewable energy technology [4]. Renewable NH_3 has the potential to replace fossil fuel in a zero-carbon emission strategy because it is a carbon-free molecule [5].

The Haber–Bosch process (HBP) was established by Fritz Haber and Carl Bosch over a century ago. The HBP is based on nitrogen fixation by involving six electrons in the nitrogen reduction reaction (NRR) process to yield NH_3 at optimal conditions [5, 6]. Despite the abundance of nitrogen in the atmosphere, the inertness of N_2 makes the synthesis of NH_3 unquestionably difficult. Breaking the N≡N bond of N_2 necessitates a tremendous amount of energy (941 kJ/mol). Along with the inertness of the bond, the competing hydrogen evolution reaction (HER) reduces the efficiency of the catalyst, ultimately reducing NH_3 yield. Due to these challenges, there is a surge of interests to design and synthesize efficient and robust electrocatalysts to expedite NH_3 synthesis [7−10].

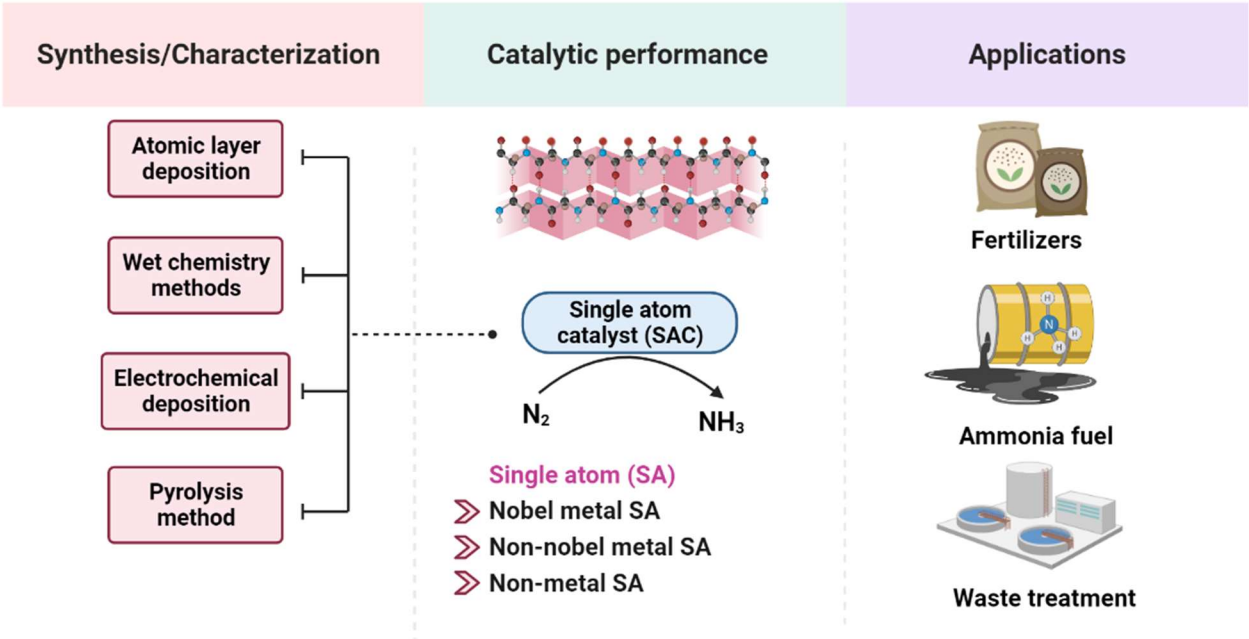

Fig. 1 Schematic illustration of the NRR with single-atom catalysts.

Recently, there is a tremendous increase in the literature reporting the catalytic potential of single atom catalysts (SACs) [11−14]. Due to their superior electronic properties, atomic assemblies, and coordination preferences, they exhibit stronger binding and activation potential as compared to their nano-scale counter parts. Several single atom catalysts have been designed, synthesized, and employed for the NRR application and found to achieve good efficiency and NH_3 yield. Advanced characterization techniques, computational techniques, and theoretical studies coupled with experimental results revealed SACs' better binding potential to N_2 and activation of the reduction at specific active sites. Using characterization and computational techniques has helped researchers explore the coordination preference of the single atoms and the mechanism of N_2 reduction. These studies not only identify the synthetic potential and structure activity relationship of the SACs and catalytic NRR but also provide great insights to suppress the competing HER and thus enhance the efficiency of NRR.

In this review, we have covered the recent advances (during the year range of 2018−2022) in the catalytic performance and efficiencies of the single atom catalysts reported for the electrocatalytic NRR. This review also discussed structure-activity relationships based on the characterizations, theoretical calculations, and experimental results. The active sites and coordination of the single atoms with the support have been discussed. Finally, the current challenges in the catalytic performance of SACs and the future prospects for the improvement in the NH_3 yield and Faradaic efficiency (FE) have been proposed.

SACs are composed of the single metal/nonmetal atoms and their support material. When the size of the active material is reduced, the amount of available active sites increases and metal-substrate interaction is enhanced, resulting in the improvement of specific catalytic activity of the metal catalyst. Electrocatalysts should thus be downsized to improve their catalytic activity in slow processes, and the simple structure of SACs makes it easier to comprehend the mechanism of the underlying reaction.

The Department of Energy of the United States has established certain execution goals for economical NH_3 generation from the NRR, such as NH_3 productivity of 10^{-4} mol h^{-1} cm^{-2} at a FE of 90% [15]. To date, a wide range of electrocatalysts have been studied (Table 1). Unfortunately, their NRR performance remains poor [10, 16−18]. For example, at NH_3 productivities of 10^{-6}–10^{-4} mol h^{-1} cm^{-2}, the FE has been limited to below 50% [19].

Table 1 Comparison of NRR catalytic performance on recently reported electrocatalysts

Electrocatalyst	Electrolyte	Potential (V *vs*. RHE)	Geometric production rate (μg cm^{-2} h^{-1})	Mass production rate (μg $mg_{cat.}^{-1}$ h^{-1})	NH_3 FE (%)	Ref.
CSA/NPC	Na_2SO_4	−0.2	14.6	—	10.5	[20]
NC-Cu SA	KOH	−0.35	—	53.3	13.8	[21]
	HCl	−0.3	—	49.3	11.7	
FeMo@NG	$LiClO_4$	−0.4	—	14.9	~10	[18]
		−0.2	—	3.4	41.7	

ISAS-Fe/NC	Phosphate buffer solution	−0.4	62.9 ± 2.7	62.9 ± 2.7	18.6 ± 0.8	[23]
Fe_{SA}-N-C	KOH	0	—	7.48	56.55	[24]
Fe-N/C-CNTs	KOH	−0.2	—	34.8	9.28	[25]
Fe-N-C	NH_4Cl	−0.05	0.9	—	4.51	[26]
SA-Mo/NPC	KOH	−0.3	—	34.0 ± 3.6	14.6 ± 1.6	[27]
P-CNTs	$LiClO_4$	−1.1	—	24.4	~0.9	[28]
Ru@ZrO_2/NC	HCl	−0.11	—	1	21	[29]
Ru/NC	HCl	−0.21	—	10.995	~8.87	
Ru SAs/*g*-C_3N_4	NaOH	0.05	—	23	8.3	[30]
Y_1/NC	HCl	−0.1	23.2	—	12.1	[31]
Sc_1/NC	HCl	−0.1	20.4	—	11.2	
Au_1Co_1@GO	K_2SO_4	−0.2	—	36.82	22.03	[32]
MoN NA/CC	HCl	−0.3	18.4212	—	1.15	[33]
NiCoS/C	$LiSO_4$	0	2.6	—	12.9	[34]
Au_1Cu_1/GCE	H_2SO_4	−0.2	—	154.91	54.96	[35]
Ru@MXene	KOH	−0.4	39.1	—	13.13	[36]
Ru_2P-rGO	HCl	−0.05	—	32.8	13.04	[37]
Bi NS	Na_2SO_4	−0.8	2.54 ± 0.16	—	10.46 ± 1.45	[38]
BNS/CP	Na_2SO_4	−0.8	—	13.22	4.04	[39]
MnO/TM	Na_2SO_4	−0.39	6.72	—	8.02	[40]
FL-BP	HCl	−0.7	—	31.37	3.09	[41]
NSs/*CF*		−0.6	—	20.87	5.07	
O-CNT/CP	$LiClO_4$	−0.4	—	32.33	12.5	[42]
BP/CP	HCl	−0.6	—	26.42	12.7	[43]
OVs-MoO_2	HCl	−0.15	—	12.2	8.2	[44]

2 Mechanistic understanding of NRR

The NRR involves (i) N_2 adsorption, (ii) different intermediate steps of electron and proton transfer, and (iii) NH_3 desorption. The NRR processes may be categorized into two routes, dissociative and associative, based on comprehensive mechanistic investigations (Figure 2) [45]. The HBP follows the dissociative route, in which the N≡N bond is completely cleaved before the reaction of hydrogen with nitrogen, necessitating an extraordinarily high energy input. For the synthesis of NH_3, the standard associative mechanism (using enzymatic pathways), as well as the dissociative process on single metal sites, have been proposed [46]. End-on adsorption for distal and alternate routes as well as side-on adsorption for the enzymatic pathway are all options for N_2 adsorption. Alternating and enzyme-catalyzed hydrogenation routes could be used for the

hydrogenation of two N_2. NH_3 is released from a far-end N atom hydrogenation in the alternating process, but a second far-end N atom is hydrogenated to make a second NH_3.

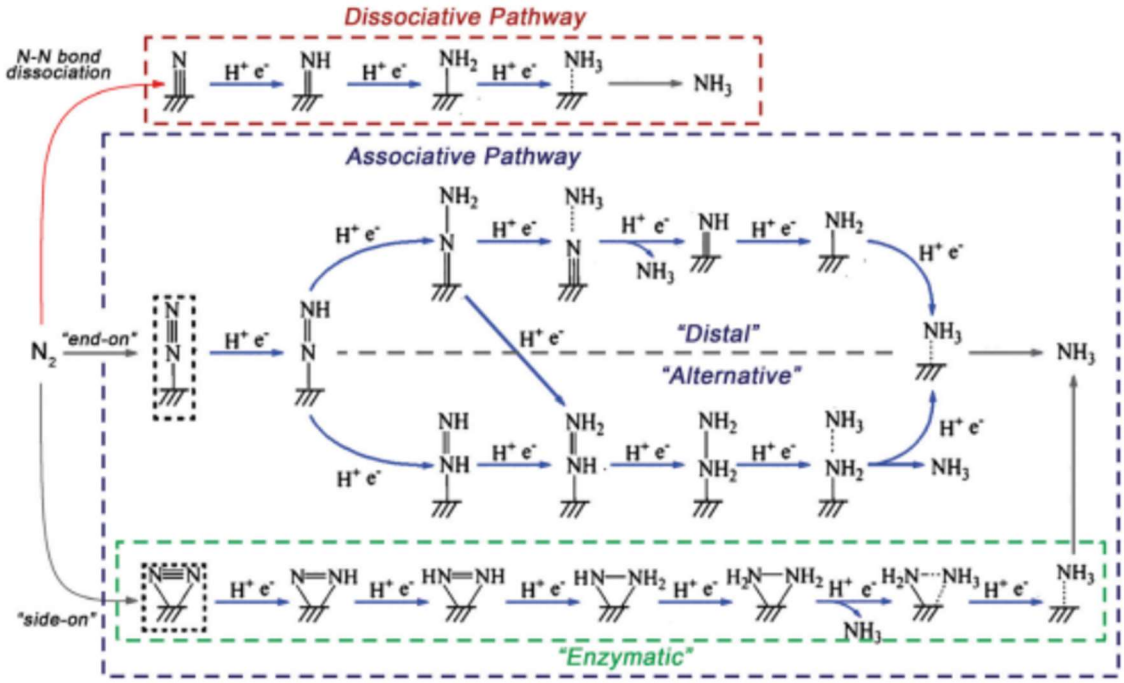

Fig. 2 Different reaction pathways including the dissociative pathway, distal and alternative associative pathway, and enzymatic pathway for NRR. Adapted with permission from Ref. [45], Copyright 2019 The Royal Society of Chemistry.

The associative route, which involves "distal", "alternating", and "enzymatic" processes, is more likely to occur under surrounding conditions. The breakdown of the N≡N bond and hydrogenation happen at the same time in this route, however, the N≡N bond is not entirely dissociated until the first NH_3 molecule is formed and released. There are two ways for N_2 to adsorb to the catalyst surface: end-on and side-on. The NH_3 release mechanism is the fundamental variation between the distal and alternate routes. The nitrogen atoms that are not attached to the surface are favorably hydrolyzed to NH_3 in the distal route. In the enzymatic pathway, however, both atoms of N_2 have equal chances of reaction with hydrogen (hydrogenation) because N_2 is

adsorbed in side-on mode, which means that molecules are equally reacting with the catalyst from both ends and the hydrogenation reaction of the N_2 atoms occurs in succession [47]. For catalysts with weak N_2 adsorption strengths, instead of N_2 adsorption, the formation of *H via the reduction of H^+ is claimed to be the first step, which subsequently initiates N_2 activation and reduction to $*N_2H_2$, followed by concerted exothermic additions of H^+ and e^- [48]. A Mars-van Krevelen pathway is put forth for the NRR on transition metal nitrides. The surface nitrogen of the nitrides is initially reduced to NH_3, forming nitrogen vacancies, which preferentially serve as further adsorption and activation sites for N_2.

When we examine the structures of the active site, we generally determine different adsorptive configurations, reactions, and activation energies for the NRR for various SACs. Wang and colleagues used first-principle calculations to investigate the catalytic behavior of the single-atom catalyst Mo_1-N_1C_2 (M = Cu, Pd, Pt, and Mo) [49]. Molybdenum single atoms anchored with N_1C_2 had greater N_2 adsorption than other metals, in both end on and side on modes with 1.18 and 1.19 eV, respectively. Mo_1-N_1C_2 used the enzymatic route; the overpotential was as low as 0.24 V, and the $*N_2$ reduction to $*N_2H$ was the potential-limiting step. As compared to the enzymatic mechanism, the alternate and distal paths have potential limiting stages, which were determined to be NH–NH_2 to NH_2–NH_2 reduction with an overpotential of 0.62 V, and NH_2–NH_2 to N_2 reduction with an overpotential of 0.57 V. These findings showed that Mo_1-N_1C_2 had a better NRR performance than other M_1-N_1C_2 structures. Furthermore, the ΔG for NH_3 desorption from Mo_1-N_1C_2 was 0.47 eV, showing that NH_3 may be quickly released from the surface in this scenario, which is good for the overall NRR.

Water is frequently used as a protic solvent in the electrochemical nitrogen reduction procedure. Many efficient metal catalysts preferentially adsorb protons over N_2 and hence have

plenty of H^+ species covering their active sites [50, 51]. Unfortunately, the HER normally takes priority on the catalyst surface because the limiting potential of NRR is negative [52]. As a result, in comparison to the HER, the aqueous NRR has poor selectivity [53]. This is because the rate-limiting step of NRR is zeroth-order dependent on proton density, whereas the HER's is first-order dependent. The efficient strategy for suppressing HER is restraining the access of protons from the electrolyte to the electrocatalyst surface; it will favor selective adsorption of N_2 on the electrocatalyst and make the hydrogenation reaction easier. Ionic liquids (ILs) and water-free donors are the potential candidates to replace the traditional electrolytes (aqueous) because it requires a very small amount of H_2O to donate H^+ and this lowers the chances of HER. To restrict the availability of H^+, MacFarlane and colleagues recommended using an aprotic, highly fluorinated IL, producing a 60% FE for the NRR. The IL exhibited good N_2 solubility as well, but its viscosity hindered N_2 transport, resulting in a low production rate of just 10^{-12} mol s^{-1} cm^{-2} [54].

The production rate of NH_3 and the FE for NRR was found to be maximal when the mole fraction of fluorinated ILs having optimum solvent-IL ratio (X_{IL}) was 0.23, with production rate and FE of 0.235×10^{-12} mol s^{-1} cm^{-2} and 32% respectively, showing the considerable role of fluorinated 1H,1H,5H-octafluoropentyl 1,1,2,2-tetrafluoroethyl ether as a solvent and highly soluble [C_4mpyr][eFAP] [55]. The selectivity and FE parameters are considerably improved by rationally designing aprotic solvents to manage H^+ adsorption. Norskov and colleagues examined the selectivity of the non-aqueous proton donor 2,6-lutidinium ($LutH^+$) and hydronium [56]. $LutH^+$ needed more energy than H_3O^+ to complete the Volmer reaction ($LutH^+ + e^- \rightleftharpoons Lut + *H$, $H_3O^+ + e^- \rightarrow H_2O + *H$), which made it even more difficult for H^+ to reach the surface of the catalyst due to the metal surface puckering. To curtail HER and improve NRR FE, non-aqueous H^+ donors are

recommended. Preventing H_2O molecules from accessing the catalyst by covering it with a water repellent layer has been shown to improve the selectivity toward NH_3 [57].

Zheng and colleagues achieved an FE of 37.8% by depositing a porous layer of polymer using Au nanoparticles (NPs) sputtered on Si-poly(tetrafluoroethylene). This hydrophobic polymer layer produced an excellent NH_3 yield of 18.9×10^{-6} g cm^{-2} h^{-1} which would not be possible without the hydrophobic poly(tetrafluoroethylene). This means that poly(tetrafluoroethylene) acted as a HER inhibitor. The resulting current density, however, was only 1×10^{-4} A cm^{-2}, which was significantly less than silicon photoanodes [58].

Thus, optimizing the different electrolytic geometries to minimize HER and increase the extent of NRR, entails two steps; (1) changing the composition of the electrolyte and (2) changing the electrode surface structure through rational design. Mass transfer and gas diffusion can be adjusted to prevent protons from making direct contact with the catalyst's surface. Additionally, the efficiency of the catalyst as well as the interaction between the electrolyte and active sites of the catalyst may be changed to increase the selectivity of the catalyst for NRR and NH_3 synthesis.

3 Single-atom electrocatalysis for NRR

3.1 Design principles of SACs for NRR

The activation of the reduction of nitrogen is an important stage in SACs catalyzed NRR. The activation of the catalytic active site on the metal SACs supported on different substrates should possess and offer an empty *d*-orbital so that it can interact with lone pair of electrons from nitrogen molecule (N_2). Because of the strong electronegativity (EN) of the ligands and other support on the catalysts, the SACs' unusual surface may result in more unoccupied d-orbitals in the metal

centers. Furthermore, the substrate's surface morphology and the functionalities exposed to the surface can significantly improve their NRR performance.

The electronic configuration of the Mo atom, for example, is $4d^5 5s^1$, with no vacant orbitals due to sp^3d^2 hybridization. Density functional theory (DFT) calculations were used by Ou et al. to build a substrate model of Mo single atom on N-doped black phosphorus (BP) ($Mo_1N_iP_{3-i}$), here (i = 0, 1, 2, 3). It has been discovered that Mo_1N_3 can chemically adsorb N_2 and that it has higher catalytic activity toward the NRR with a very low overpotential of 0.02 V through the associative distal mechanism, suggesting that it can catalyze the NRR in an ambient environment. Moreover, Mo_1N_3 exhibits good stability for NRR intermediates as well as the quick elimination of the generated NH_3 with only 0.56 eV free energy [54]. Because of the high EN values of the atoms adhered, it allows them to accept lone pair of electrons from N_2 in *d*-orbitals and electrons from Mo orbitals. Only Mo_1N_3 and the intermediate reactant N_xH_y exchanged electrons in the first three stages, whereas BP was involved in the last steps to facilitate the synthesis and removal of the second NH_3 molecule [59].

Li and colleagues examined and investigated the NRR performance of FeN_4- and FeN_3-embedded graphene (Gr) in more detail (Figure 3a−f). After the interaction of FeN_4 with graphene, the dipole moment is converted into two (lower and upper) components, the lower value of the dipole moment of the interaction center makes it hard to polarize N_2 [47] . In FeN_3, the dipole moment of iron is increased from 0 to 3.16 μ_B after N-doping in a single vacancy. The greater dipole moment resulted in the distribution of a more concentrated electron cloud in the vicinity of iron atoms toward the left-center of the Gr-layer, showing that FeN_3-Gr is very important for N_2 adsorption. After adsorption of N_2, the electron cloud distributed evenly on N_2-FeN_3 and this indicated that N_2 had been activated.

Sabatier's principle shows (Figure 4a) the interaction of the reactants in the presence of a catalyst. These interactions should not be too strong or too weak. If the connection between the reactants and the catalyst is too strong, then it will be difficult to desorb products, and vice versa for a weak interaction. On the left side of the plot, product removal is limited because of the high bond strength. The product becomes more prone to desorption for weak bond strength and the rate gradually increases. On the right side of the plot, activation of the reactants is not very easy, and the catalytic rate decreases as the bond strength become weak [60]. The reactants become easier to activate as the bond strength improves, and the rate will eventually increase. As a result, the volcano plot's maximum correlates to the strongest bond strength and maximum activity. On the other hand, this principle does not describe the bond strength of reactants and catalysts in the intermediate state.

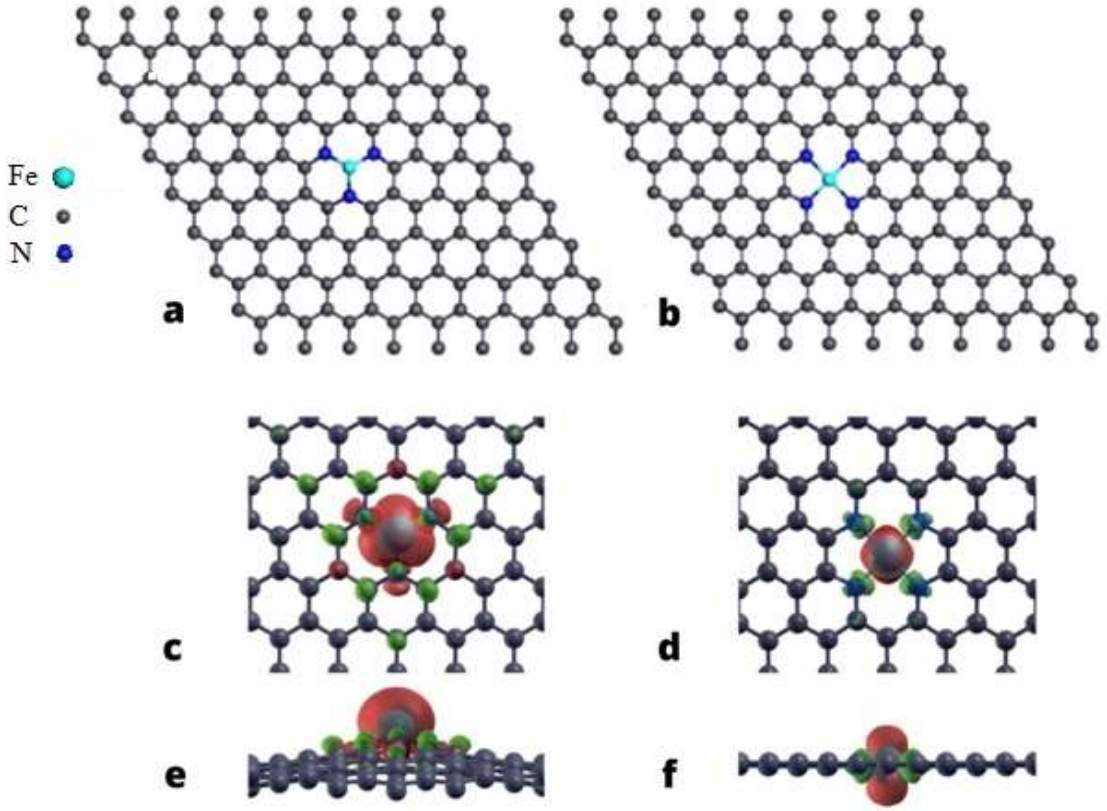

Fig. 3 Two optimized structures of (a) FeN_3-Gr and (b) FeN_4-Gr are considered and the pictures of isosurfaces of spin-resolved density showing the top views of (c) FeN_3-Gr and (d) FeN_4-Gr and side views of (e) FeN_3-Gr and (f) FeN_4-Gr. Adapted with permission from Ref. [47], Copyright 2016 American Chemical Society

The linear scaling connection between the energetics of two intermediates, $*N_2H$ and $*NH_2$, as illustrated in Figure 4b, was proposed by Montoya et al. as a novel perspective on the significance of nitrogen scaling relationships in the electrochemical synthesis of NH_3 [61]. The performance of the electrochemical and gas-phase catalysts can be improved by employing metal alloys but the binding configurations of the important adsorbates e.g., $*N_2H$, *NH, and $*NH_2$ (where adsorption occurs on single atom catalyst coordinated with N atoms) are almost similar. Thus, it is almost impossible to break the scaling relationship of the NRR. Surfaces having bifunctional ability to bind $*N_2H$ and $*NH_2$ onto distinct active sites, or having numerous sites, would allow the scaling relationships to be broken, allowing for an effective heterogeneous catalyst for the electrochemical production of NH_3 [62].

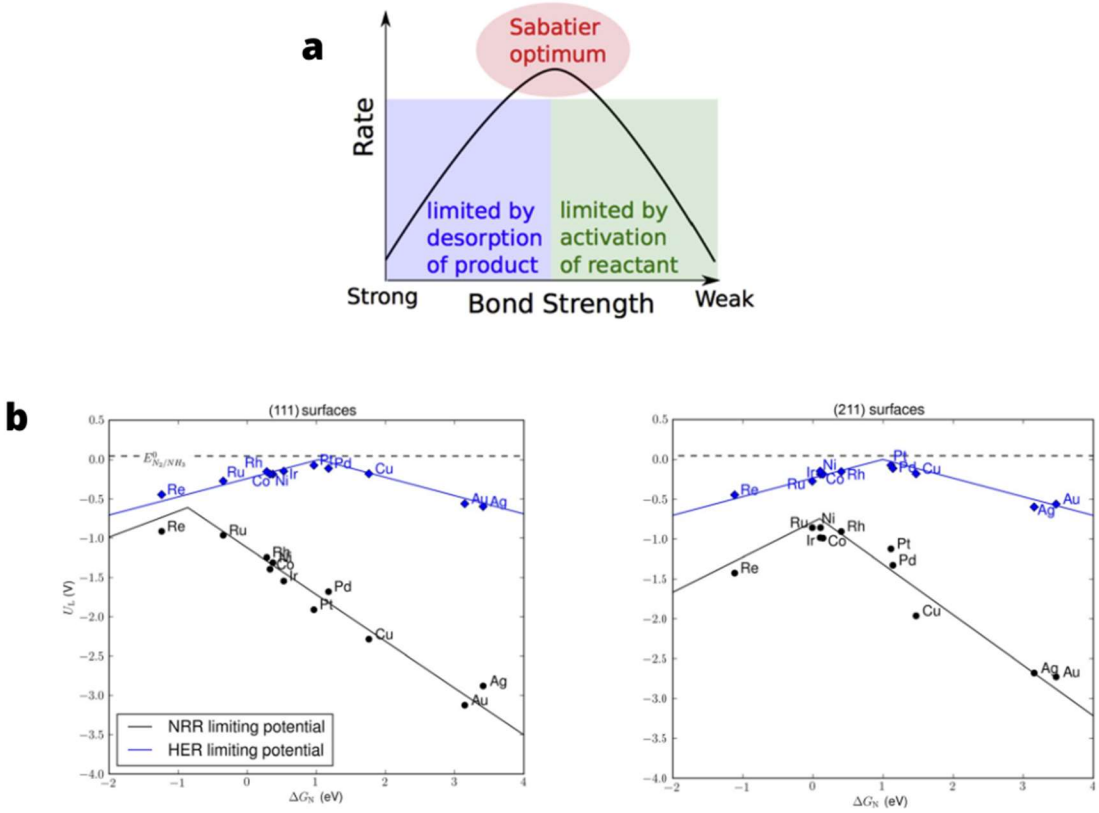

Fig. 4 (a) Illustration of qualitative Sabatier principle. Adapted with permission from Ref. [60], Copyright 2015 Elsevier. (b) Comparison of HER and NRR limiting-potential volcanoes. The HER and NRR overpotentials as a function of the *N binding-energy energy descriptor is shown in blue and black, respectively, and individual metal points are labeled for (111) (left) and (211) (right) surfaces. Here from the graph, it is clear that HER limiting potentials are consistently less negative than those for NRR. Adapted with permission from Ref. [61], Copyright 2018 American Chemical Society.

3.2 SACs synthesis techniques

The appropriate synthetic procedures are essential for fabricating high-quality SACs due to the aggregation potential of metal ions that result from the high surface energy of single metal atoms on supports. There have been several advancements in the synthesis of SACs in recent years [63]. The large-scale production and the instability of SACs still pose substantial challenges, despite

this, SACs may be synthesized using both bottom-up and top-down approaches. There are several methods of bottom-up synthesis, including co-precipitation and atomic layer deposition (ALD), that exploit defects or vacancies on support materials to anchor metals from decomposed metal-containing precursors [64−66].

3.2.1 Atomic layer deposition

ALD is a chemical precursor-based pulse vapor deposition technique. By methodically altering the number of deposition cycles, this method may accurately control the size, shape, loading, and active site distribution of SACs [67]. Usually, SACs processed by ALD contain loadings of less than 2% by weight [68].

Sun and colleagues employed this method to manufacture a platinum (Pt) single-atom catalyst using a Pt precursor and O_2 [69]. The $MeCpPtMe_3$ ligand reacted with the oxygen functional groups present on the graphene nanosheets to generate a Pt monolayer. The Pt surface was then exposed to oxygen, forming a fresh layer of oxygen species on the surface that reacted with $MeCpPtMe_3$ in the following cycle (Figure 5a). As a result, the number of ALD cycles may be adjusted to accurately control Pt deposition.

Similarly, Lei and colleagues demonstrated the use of very thin metal oxide protective coatings created by ALD to stabilize single-atom Pd catalysts (Figure 5b) [70]. ALD was used to chemisorb palladium hexafluoroacetylacetonate (hfac) on the surface of alumina. ALD was then used to deposit ultrathin TiO_2 coatings onto the substrate. To produce nanocavities, the TiO_2 layer was deposited selectively on the surface without palladium hexafluoro acetylacetonate. After eliminating the hfac ligands with formalin, the Pd SACs were produced in the TiO_2 nanocavities.

3.2.2 Wet chemical method

Simple processes are used in wet chemical approaches, which show promise for large-scale SACs synthesis. Usually, two processes in succession are used to consistently anchor single metal atoms (SMAs) to their support. In the liquid phase, the hydrothermal process is utilized to bind metal atoms to the support or to decrease metal ions to single atoms. To obtain SACs, freeze-drying techniques and gas-phase reduction methods are used [46].

For example, Fei et al. used a combination of graphene oxide, metal precursor, and H_2O_2 hydrothermally with hydrogels of metal-doped graphene oxide as SAC precursors (Figure 5c) [71]. This gel was heated at 900 °C in an NH_3 environment after being freeze-dried. The metal atoms were then uniformly attached in an MN_4C_4 coordination arrangement on the N_2-doped graphene surface. Choi and colleagues have synthesized a Pt catalyst on zeolite templated carbon (ZTC) with a high percentage loading of Pt (5 wt%) via wet chemical method [74]. At 823 K, acetylene/H_2S chemical vapor deposition was used to make sulfur-doped ZTC in a NaX zeolite template. The Pt catalysts were then impregnated in the ZTC using H_2PtCl_6.

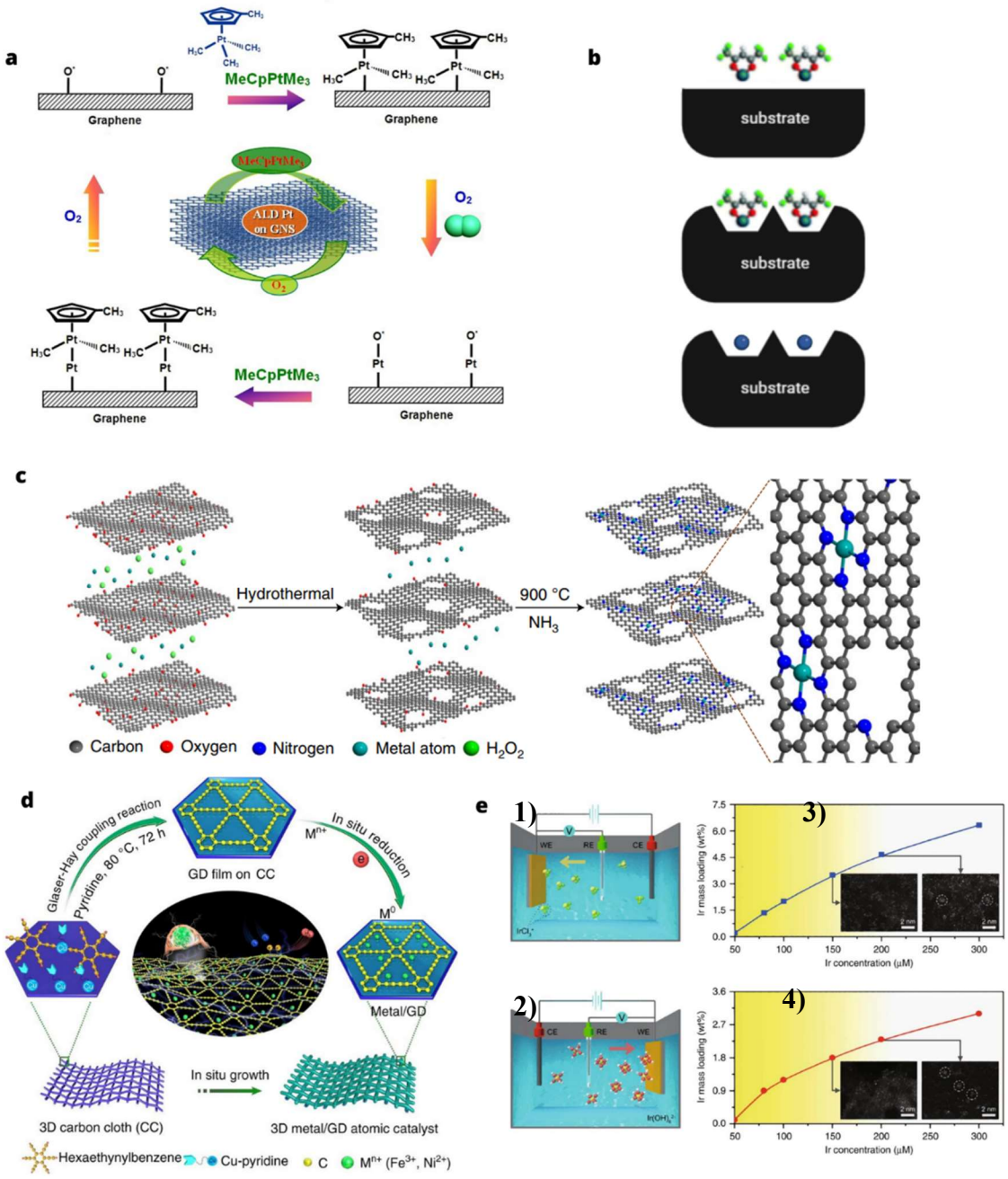

Fig. 5 (a) Schematic illustrations of the mechanism of Pt ALD on graphene. Adapted with permission from Ref. [69], Copyright 2013 Springer Nature. (b) Schematic of thermally stable Pd catalyst synthesized using ALD. The figure is redrawn from Ref. [70]. (c) Schematic of metal SACs on graphene oxide (GO). The GO solution was hydrothermally processed in hydrogen peroxide and metal precursors to generate a 3D GO hydrogel. After freeze-drying the hydrogel, the GO was reduced further, and N-dopants were incorporated into the 2D-GO lattice using a thermal method in an ammonia environment. Adapted with permission from Ref. [71], Copyright

2018 Springer Nature. (d) Schematic of synthesis of Ni/graphdiyne and Fe/graphdiyne (GD). This is a two-step approach where GD layers were grown in situ on 3D-carbon cloth (CC) surfaces and resulted in the reduction of metal ions (Ni^{2+} and Fe^{3+}) to metal species with zero valances [Ni (0) and Fe (0)]. Adapted with permission from Ref. [72], Copyright 2018 Nature Publishing Group. (e) Deposition of iridium species. Panels 1) and 2) show the cathodic and anodic electrochemical deposition mechanism, respectively. Iridium mass loadings as a function of iridium concentration in the 1 M KOH electrolyte for cathodic 3) and anodic 4) deposition. The cycle number of scanning was set at 10 and 3 for cathodic and anodic deposition respectively. Adapted with permission from Ref. [73], Copyright 2020 Nature Publishing Group.

3.2.3 Electrochemical deposition (ECD)

By controlling the metal precursor concentration and deposition period, ECD techniques can modify the loading, coordination, and density of the active site of SACs. Reduced metal ion diffusion rates usually result in the formation of single-atom structures on the substrate [72].

Xue and colleagues used a two-step technique to create nickel/graphdiyne and iron/graphdiyne SACs (Figure 5d). The first step was the cross-coupling reaction of acetylene with hexaethynylbenzene as a precursor to build 3D graphdiyne foam on the carbon cloth surface. Then, using a simple electrochemical reduction process, Ni and Fe atoms were attached to the graphdiyne foam [72]. Zhang and colleagues also presented a universal ECD approach for synthesizing over thirty different types of SACs (Figure 5e). To generate distinct single-atom structures, they used different types of metals and also altered the deposition reactions that take place at the anode and cathode [73]. To make the metal precursor, the authors combined iridium tetrachloride ($IrCl_4$) with a KOH aqueous solution. Iridium single metal catalysts could then be made using both cathodic and anodic deposition techniques. Ir-SACs were generated at the cathode by deposition of $IrCl^{3+}$; at the anode, $Ir(OH)_6^{2-}$ was the precursor of Ir-SACs created on cobalt hydroxide nanosheets.

Hence, the deposition rate of metal precursors can be controlled by adjusting the electrochemical current.

3.2.4 Pyrolysis method

The pyrolysis process is a commonly used method for creating atomically distributed compounds by decomposing different precursors at high temperatures in a gaseous environment (such as Ar and NH_3) [75−78]. Metal complexes, polymers, metal-organic frameworks (MOFs), and other precursors can all be used to make atomically dispersed catalysts [79−83]. This approach offers several advantages, including ease of use and low-cost raw materials. The production of nanoparticles and nanoclusters with significant metal loading, on the other hand, remains a major difficulty. This process has been used to make the majority of carbon-based electrocatalysts with single metal sites to date.

A comprehensive comparison of the general properties of the various SAC synthesis methods is summarized in Table 2. ALD can provide fine control by using costly and precise equipment. Simple techniques and equipment are used in wet chemical treatments. By varying the current, ECD can control the rate of deposition. At the expense of a higher temperature environment, pyrolysis can produce great structural and metal loadings. To avoid the aggregation of atoms and maximize the yield of SACs, it is critical to improve the various synthesis processes according to their respective properties.

Table 2 Comparison of different SAC synthesis methods

Synthesis method	Merit
Atomic layer deposition	Precise control of the SACs synthesis process
Wet chemical method	Simple operation and potential for commercial SACs synthesis

Electrochemical deposition	Controllability of the deposition rate by altering the electrochemical current
Pyrolysis method	High structural stability and metal loading

3.3 SACs explored for NRR

SACs are made up of isolated single atoms with distinct electronic configurations that enhance their electrocatalytic activity in a variety of processes. The facile activation of the nitrogen molecule is a major challenge due to the higher intrinsic stability of the triple bond. The catalytic activity of the NRR process could be considerably improved using SACs compared to their respective NPs due to the atomic scale and their superior electronic properties [68]. The positively charged SACs make the metal *d*-orbitals polarized, which subsequently improves the NRR by enhancement of the binding potential to N_2 and suppress the HER by the reduction in H-adsorption. The higher NRR and lower HER render SACs as promising candidates for higher NH_3 production efficiency and FE. There are three types of SACs for the NRR, as illustrated in Figure 6 and described below [84].

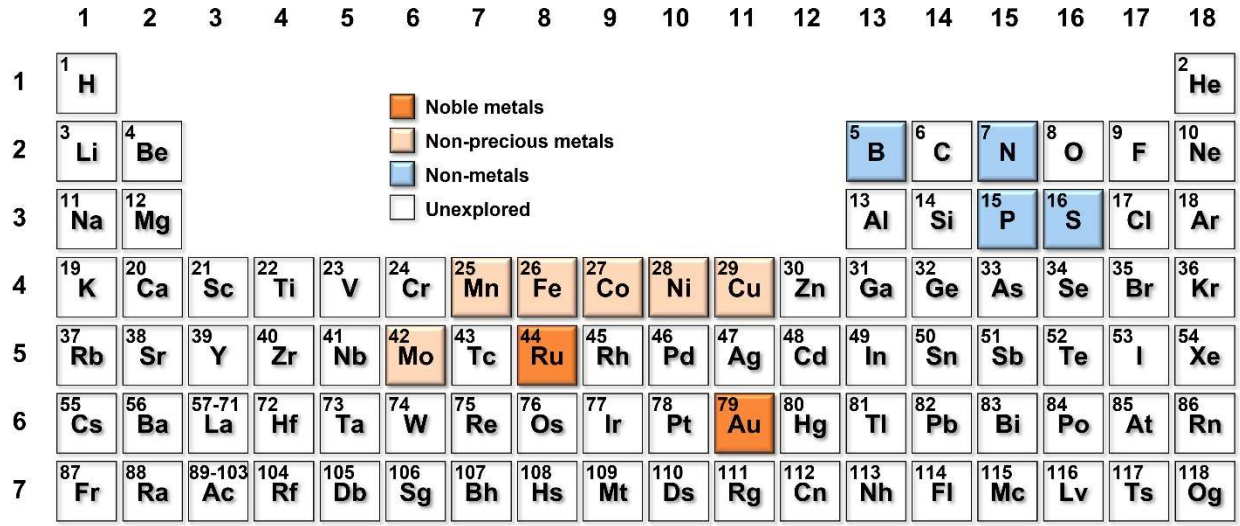

Fig. 6 Illustration of single atom elements used for NRR in periodic table.

3.3.1 Noble metal SACs for NRR

3.3.1.1 Ru SACs

3.3.1.1.1 Ru-N sites

Among the experimental studies conducted using noble-metal SACs, Ru SACs have been found as efficient catalysts for NRR. Geng et al. synthesized Ru SACs supported on N-doped carbon (Ru/N-C) via pyrolysis. The highest FE of the Ru-N_3 coordination catalyst was observed in Ru/N-C. The catalyst having Ru-N_4 coordinated active sites afforded the NH_3 yield of 120.9 μg h^{-1} mg_{cat}^{-1} with the highest FE of 29.6% (Table 3, entry 1). The DFT calculations suggested a strong binding of N_2 to Ru/N-C catalyst that further undergoes reduction via the distal pathway on Ru-N_3 active sites that promote dissociation of N_2. Moreover, the characterization results from thermal diffuse scattering images of electrocatalysts made of Ru single atoms have higher chemisorption of nitrogen than the catalyst made of Ru NPs. Because of this advantage, the Ru SAs/N-C electrocatalyst has lower Gibbs free energy (GFE) for the rate-determining step (RDS) of the NRR than the Ru NPs/N-C catalyst. The lower GFE of RDS made this electrocatalyst good for NRR and synthesis of NH_3. Suppressing the H_2 evolution to lower the fraction of electrons involved in this competing process is thought to be an effective way to improve NH_3 selectivity [85].

In addition to the above, Tao et al. synthesized a single atom catalyst (Ru/N-C) using Ru SACs supported on N-doped porous carbon via a coordination-assisted strategy. The catalyst exhibited a maximum NH_3 yield efficiency of 3665 μg h^{-1} mg_{cat}^{-1} with an FE of ~7.5% (Table 3, entry 2). The Ru-NC_2 species were claimed to be major active sites due to their lower free energy for NRR compared to other Ru-N_xC_y sites (Ru-N_2C, Ru-N_3, Ru-NC_3, Ru-N_2C_2, Ru-N'_2C_2, Ru-N_3C, and Ru-N_4). Tao et al., also synthesized Ru@ZrO_2/N-C catalyst by Ru SACs supported on N-doped porous carbon introduced with ZrO_2 moiety. The catalyst was also found to be very active for ambient

electrocatalytic reduction of N_2. The introduction of ZrO_2 suppressed the competitive HER, and the FE of the catalyst increased significantly to 21%, but the NH_3 yield decreased (~1700 μg h^{-1} mg_{cat}^{-1}). The inhibition of HER and higher FE were observed due to the Ru single atom active sites with oxygen vacancies in Ru@ZrO_2/N-C. According to DFT calculations, the N_2 reduction reaction took place mostly at Ru sites with "O" vacancies, and their high catalytic performances were due to the stabilization of *NNH (low overpotential), dramatic destabilization of *H (high NRR/HER selectivity), that activates the NRR process. The Ru atoms with oxygen vacancies enhanced N_2 adsorption, stabilization of *NNH, and destabilization of *H. Moreover, the Ru-$Zr_{32}O_{63}$ improved the selectivity of the $*N_2/*H$ as the "O" vacancies in ZrO_2 effectively inhibited isolated Ru atoms from aggregating (Table 3, entry 3). [29, 86]

3.3.1.1.2 Ru-O sites

Chen et al. synthesized an electrocatalyst of Ru-SAs/Ti_3C_2O via a simple chemical-assisted technique. In the Ru-SAs/Ti_3C_2O catalyst, Ru single atoms were immobilized on the surface of Ti_3C_2O substrate and investigated for NRR activity. The results of X-ray photoelectron spectroscopy (XPS) on NH_3 confirmed the successful activation of O-termination groups. With the use of high-angle annular dark-field scanning-mode transition electron microscopy (HAADF-STEM), atoms adsorbed on Ti_3C_2O substrate were directly detected. A desirable NH_3 yield rate of 27.56 μg h^{-1} mg_{cat}^{-1} was achieved using the catalyst and a FE of 23.3% at a low potential of −0.2 V relative to a reversible hydrogen electrode (RHE) (Table 3, entry 6). The DFT studies in combination with the characterization suggested coordination of Ru with oxygen and revealed that the Ru-O_4 active sites are responsible for the N_2 activation through a novel distal/alternating hybrid pathway. The electrocatalytic NRR occurred via a hybrid path, in which the $*NNH_2$ was hydrogenated to $*NHNH_2$, and the energy required was significantly lowered. By removing the

potential-limiting phase's barrier, the potential-limiting step can be completed more quickly. The dynamics of the NRR for this work not only presents a straightforward and easy-to-understand but also an effective technique for synthesizing atomically distributed single atom catalysts, paving the way for more efficient N_2 reduction in natural conditions, but it also opens a thrilling new world toward the direction of NRR [87].

3.3.1.1.3 Ru-C sites

Peng et al. synthesized the electrocatalyst SA Ru-Mo_2CT_x by incorporating the ruthenium single atoms into the Mo_2CT_x MXene nanosheets (Table 3, entry 7). The catalyst achieved a promising NH_3 yield of 40.57 μg h^{-1} mg_{cat}^{-1} and an FE of 25.77% in 0.5 M K_2SO_4 solution at −0.3 V (*vs*. RHE). DFT and operando X-ray adsorption studies revealed that Ru SAs anchored on the surface of MXene nanosheets served as the active sites for N_2 activation via electron back donation. The SA Ru-Mo_2CT_x possessed abundant Ru-C(O) active sites for NRR application which not only promoted N_2 adsorption and activation but also lowered the energy barrier for the first hydrogenation step [88].

HER and NRR are two competing reactions, and better efficiency could be achieved by promoting the NRR and the inhibition of HER. Ru SAs coordinated to N, O, and S, have been known to be good catalysts for NRR, so the conjugation of a HER suppressing agent can render Ru SACs with efficient activity for the NRR. Ru-N-rich coordination can increase the NRR performance and the introduction of a supporting scaffold such as ZrO_2 for the suppression of HER can thus further enhance the activity. Furthermore, among the Ru SACs, the catalyst with the Ru-N coordination showed the highest efficiency for NRR, followed by Ru-C(O) and Ru-O coordination. N-rich coordination can increase NRR performance.

3.3.1.2 Au SACs for NRR

3.3.1.2.1 Au-N sites

Au-based SACs have also been researched extensively due to their low theoretical affinity for hydrogen, which is projected to limit the HER activity while increasing the NH_3 FE.

Wang and colleagues synthesized a single atom electrocatalyst Au_1-C_3N_4 by atomically dispersing Au SAs on a carbon nitride support (Au_1-C_3N_4) along with its nanoparticle counterpart (Au NPs-C_3N_4) [89]. The potential of the developed catalyst for NRR application was evaluated and compared with each other. The highest activity among the two catalysts was observed for Au-C_3N_4 catalyst having Au-N_3 active sites. It achieved a higher NH_3 yield rate of 1305 μg h^{-1} mg_{cat}^{-1} and a FE of 11.1% (Table 3, entry 4). The NH_3 yield rate obtained for Au_1-C_3N_4 was around 22.5 times higher than that of Au NPs-C_3N_4. DFT calculation proposed that Au_1-C_3N_4 catalyzed via an alternating hydrogenation process, requiring a lower energy in the first hydrogenation step. Moreover, in a two-electrode electrolyzer with an energy consumption rate of 4.02×10^{-3} mol k/J, a by-product-free synthesis of NH_3 from N_2 and H_2 was achieved using the Au_1-C_3N_4 catalyst [89].

The performance of SACs is also greatly influenced by achieving the best possible coordination between the substrate and single atoms. Qin and colleagues developed an electrocatalyst Au SAs-NDPCs made up of Au single sites anchored on N-doped porous carbons for the NRR [90]. The catalyst delivered a stable and promising NH_3 yield of 2.32 μg h^{-1} mg_{cat}^{-1} and a FE of 12.3% (Table 3, entry 5). Further characterization and DFT calculations suggested that the positively charged Au atoms acted as Lewis acid sites while the electron rich nitrogen atoms acted as Lewis base sites forming frustrated Lewis pairs (FLPs) that promoted the activation of N_2 for NH_3 production [90]. The Au SAC coordinated with three nitrogen atoms resulted in a

significantly higher NH_3 yield than the frustrated Lewis pair interaction between the Au SAC and nitrogen atom, however the FEs of both catalysts are comparable to each other.

Other coordination structures of Au SACs for NRR are still lacking, warranting further exploration. It is expected that the NRR performance of Au SACs can be further improved by tuning and optimizing the bond microenvironments of Au with other heteroatoms (e.g., C, O, or S).

3.3.2 Non-precious metal SACs for NRR

Noble metal-based catalysts have limited applicability due to their high prices and limited reserves. The SACs of non-noble metals (NNM) offer significant promise as very good catalysts for the NRR and are economical as well. Transition metal (TM)-SACs are active electrocatalysts for the NRR, because TMs can donate electrons to the antibonding orbitals of nitrogen and meanwhile the nitrogen adsorption on the active sites of TM is boosted by transferring electrons to the unoccupied *d* orbital of a TM. As a result, TMs having both unoccupied and occupied *d*-orbitals become very efficient NRR electrocatalysts. Iron and molybdenum are essential metals for the natural nitrogen fixation processes and Fe is also a very effective catalyst for the HBP. Finding efficient and durable electrocatalysts to speed up the NRR is critical [91−93]. In general, the yield rate and FE of NH_3 evolution, as well as catalyst stability, are the most important indicators for evaluating NRR catalysts, which are measured using ammonia quantification techniques such as indophenol method, NMR, and ion chromatography [94, 95]. These theories, when paired with DFT calculations, show that NNM based SACs have a lot of promise as NRR electrocatalysts.

3.3.2.1 Cu SACs (Cu-N sites) for NRR

Although atomically dispersed catalysts based on Cu have been extensively explored in electrocatalytic oxygen reduction reaction and CO_2 reduction reaction, single-atom Cu catalysts

have been rarely used in NRR [96−98]. Kou and colleagues synthesized Cu SAC, which was for the first time applied for NRR by incorporating Cu SAs to porous nitrogen-doped carbon substrate *via* a surfactant-assisted synthesis method [21]. Strong interaction between isolated Cu atoms and supports is critical for the rational design of atomically dispersed Cu-based catalysts. DFT calculations revealed that the catalyst achieved comparable activity due to the high density of exposed Cu-N_2 active sites (Table 3, entry 8). In an alkaline situation, the derived NC-Cu SAC was able to catalyze NRR at potentials from 0.25 to 0.5 V (*vs*. RHE), and the greatest NH_3 production rate was $53.3 \pm 1.86 \times 10^{-6}$ μg h^{-1} mg_{cat}^{-1} with a FE of 13.8% using 0.1 M KOH as catholyte at 0.35 V (*vs*. RHE). Isotopic labeling experiments further demonstrated that the NH_3 produced originated from N_2 electroreduction, and the NC-Cu SAC exhibited an excellent stability in 0.1 M KOH. This catalyst is pH universal and is flexible to use over a large pH range. Furthermore, in an acidic environment, NC-Cu SAC showed higher activity and stability. In 0.1 M HCl, the NH_3 yield rate was 49.3 ± 0.70 μg h^{-1} mg_{cat}^{-1} and the FE was 11.7% at 0.3 V (*vs*. RHE), but after eight cycles, the FE declined from 11.7% to 9.8%. This catalyst is pH universal and is flexible to use over a large pH range. Theoretical calculations proposed that Cu-N_2 species was the catalytic site for N_2 activation, while Cu-N_3 and Cu-N_4 sites were not active for the NRR. For the reduction of N_2 on Cu-N_2 active site, the energy barrier was calculated to be 1.573 eV and NRR proceeded *via* distal and alternating pathways [21]. Despite these Cu-N sites for enhanced NRR, other tailored bond configurations (such as Cu-C and Cu-O coordination structures) need to be explored for N_2 adsorption and activation, which would be an interesting topic.

3.3.2.2 Fe SACs for NRR

Fe-based electrocatalysts are also anticipated to accomplish effective ammonia synthesis since iron is the active core of both the HBP and natural biological nitrogenase. In general, the yield rate and

faradaic efficiency of NH_3 evolution, as well as catalyst stability, are the most important indicators for evaluating NRR catalysts, which are measured using ammonia quantification techniques such as ion chromatography [12, 94, 99]. However, because the potential of the HER is near zero, keeping the NRR potential within a tolerable range can effectively limit the HER and increase the FE of NH_3 formation. Prior theoretical analyses demonstrated the feasibility of atomically distributed Fe-based catalysts for the NRR.

3.3.2.2.1 Fe-N sites

DFT simulations suggested that the atomically dispersed FeN_3 active sites for NRR may be attributed to the FeN_3 moiety's high-spin polarization [47]. Furthermore, Fe magnetism had a significant effect on N_2 activation [100-103].

Lu et al. synthesized isolated single Fe atomic sites incorporated to N-doped carbon framework (ISAS-Fe/NC) electrocatalyst by atomic dispersion of Fe single atoms on N-doped carbon frameworks for NRR applications. The electrocatalytic performance of ISAS-Fe/NC was evaluated in 0.1 M phosphate-buffered saline (PBS), which exhibited a considerable NH_3 yield of 62.9 μg h^{-1} mg_{cat}^{-1} and a high FE value of 18.6% at −0.4 V (*vs*. RHE) under ambient conditions (Table 3, entry 9). Furthermore, ISAS-Fe/NC was shown to be stable with no evident decline in activity for 24 hours, suggesting that NH_3 was created from N_2 *via* NRR supported by the isotopic labeling experiments with $^{15}N_2$. Structural characterizations revealed that Fe SAs were stabilized by coordination with four N atoms and Fe-N_4 site was found to be favorable for N_2 reduction. During N_2 reduction, electrons shift from Fe (3*d* orbital) to N (2*p* orbital) which further activates N_2 reduction [23]. For efficient ammonia synthesis via NRR, another electrocatalyst containing Fe single atoms anchored on N-doped carbon (Fe SAs/N-C) was reported by Wang et al. Using the developed electrocatalyst, a high FE value of 56.55% was achieved along with a corresponding

NH_3 yield efficiency of 7.48 μg h^{-1} mg_{cat}^{-1} (Table 3, entry 10). Molecular dynamic studies suggested the efficient access of N_2 molecules to Fe SAs for adsorption followed by reduction. The binding of N_2 molecule to Fe-N_4 active sites was found to be exothermic with a binding energy of −0.28 eV. Characterization revealed that Fe single atoms were equally spread across the graphene surface. Nitrogen with a high concentration was 0.45 nm distant from the Fe sites, which aided in the subsequent adsorption of NRR on active sites. Furthermore, as compared to the distal pathway, the alternate pathway was a more compelling mechanism on extensively scattered Fe sites [24]. Similarly, another noble metal-free catalyst was designed and developed by anchoring Fe SAs on the N-doped carbon nanotube substrate (Fe-N/C-(CNT)) that was derived from metal-organic framework and carbon nanotube-based composite. The catalyst achieved an NH_3 yield of 34.83 μg h^{-1}·mg_{cat}^{-1}, and a FE of 9.28% (Table 3, entry 11). This catalyst was found to be selective, efficient, and stable under ambient and aqueous conditions. Experimental and theoretical studies revealed that Fe-N_3 was the primary active site present in the developed catalyst for N_2 reduction [25].

Zhang et al. reported Fe SAs incorporated in N-doped carbon (Fe_1/N-C), which was prepared *via* a mixed ligand strategy by employing Fe SAs decorated metal-organic framework as a precursor. Due to the high dispersion of Fe SAs, the porous nature of the carbon substrate, and the conductivity of the N-doped carbon substrate, the catalyst Fe_1/N-C achieved an NH_3 yield of 1.56 × 10^{-11} mol cm^{-2} s^{-1} and a FE of 4.51% (Table 3, entry 12). Theoretical studies predicted that the Fe_1-N-C exhibited the lowest energy barrier for N_2 reduction during the rate determining step, consistent with the experimental results. Moreover, among the various Fe-N_x sites, the Fe-N_4 site was found to be catalytically active for the NRR [26, 104].

3.3.2.2.2 Fe-O sites

Zhang et al. reported two electrocatalysts, Fe-SAs/LCC/CC and Fe-SAs/LCC/GC. Fe SAs were anchored on the lignocellulose-derived carbon (LCC), which was mounted on the surface of porous carbon (CC) and glassy carbon (GC) to fabricate Fe-SAs/LCC/CC (Table 3, entry 20) and Fe-SAs/LCC/GC (Table 3, entry 21), respectively. Fe-SAs/LCC/GC (307.7 μg h^{-1} mg_{cat}^{-1}) was found to have a superior NH_3 yield than Fe-SAs/LCC/GC (32.1 μg h^{-1} mg_{cat}^{-1}). Moreover, Fe-SAs/LCC/GC achieved a higher FE value of 54.1% at −0.05 (*vs*. RHE) as compared to the Fe-SAs/LCC/CC catalyst. Fe-$(O\text{-}C_2)_4$ was revealed as the active sites for N_2 reduction. The adsorption of N_2 on the surface of Fe occurred *via* a back donation mechanism. The superior catalytic activity of the Fe-SAs/LCC/GC was supported by electrochemical impedance spectra (EIS) results, which showed the charge transfer resistance of the Fe-SAs/LCC/CC (3.58 W) was more than two-fold higher than that of Fe-SAs/LCC/GC (0.013 W). Furthermore, the catalyst loaded on porous carbon CC distributed throughout the 250 mm thick CC substrate, while in the case of GC the catalyst only formed a uniform and thin layer of 12 mm at the surface of the GC substrate. Enhanced catalytic performance of Fe-SAs/LCC/GC was attributed to the thin layer due to the strong adsorption and good transport of N_2 [105].

Su et al. reported another single atom catalyst that was developed by atomic dispersion of Fe SAs on MoS_2 nanosheets (Fe/MoS_2) for N_2 reduction to NH_3 at room temperature. Fe/MoS_2 exhibited an NH_3 FE of 18.8% and NH_3 yield of 8.63 μg h^{-1} mg_{cat}^{-1} (Table 3, entry 22). It was revealed that the S edges in MoS_2 decorated with Fe SAs promoted the NRR by suppressing the competing HER. An Fe atom was found to coordinate with 3 oxygen atoms (due to oxidation) and one S atom, which facilitated N_2 adsorption *via* a hybrid pathway [106].

3.3.2.2.2 Fe-S sites

Fe SAs were synthesized by Li et al. to decorate on the surface of atomically thin MoS_2 nanosheets to obtain Fe/MoS_2 (Table 3, entry 23). The catalyst involved the mechanism of interfacial polarization that promoted the N_2 reduction to NH_3. The Fe SAs coordinated with three S atoms. The Fe SA protrusions anchored on the surface of MoS_2 nanosheets stimulated the electric field that polarized the N_2 molecule and substantially accelerated the electron transfer from Fe SAs to N_2. Due to this efficient interfacial polarization, the catalyst achieved a high NH_3 yield of 97.5 μg h^{-1} mg_{cat}^{-1} and a FE of 31.6% at an applied potential of −2.0 V (*vs*. RHE) [107].

Although different types of Fe SACs have been designed and evaluated for the NRR, the best coordination structure remains unclear. Therefore, further endeavors need to be made on a detailed study on the NRR performances of various Fe single atom structures under equivalent reaction conditions.

3.3.2.3 Co SACs (Co-N sites) for NRR

Gao et al. developed a Co single atom electrocatalyst Co/N-C by dispersion of Co SAs on N-doped carbon composites for N_2 fixation at ambient conditions. The catalyst possessed Co-N_x catalytic sites for activation of the adsorbed N_2. The Co/N-C catalyst yielded an NH_3 formation rate of 5.1 μg_{NH3} h^{-1} mg_{cat}^{-1} with a FE of 10.1% (Table 3, entry 13). Experiments combined with theoretical calculations suggested that Co single atoms coordinated with the pyrrolic N served as major active sites for N_2 activation and reduction [22]. In addition to Co-N sites, other Co SACs with different coordination structures and supports are the focus of future research interest for the NRR.

3.3.2.4 Ni SACs (Ni-N sites) for NRR

Mukherjee et al. used Ni SAs to develop Ni-N_x-C catalyst in which Ni single atoms were atomically dispersed on a N doped carbon substrate (Table 3, entry 14). The catalyst achieved an

optimal NH_3 yield rate of 60 μg h^{-1} mg_{cat}^{-1}, 85 μg h^{-1} mg_{cat}^{-1} and 115 μg h^{-1} mg_{cat}^{-1} when performed in 0.1 M HCl, 0.1 M KOH, and 0.5 M $LiClO_4$, respectively. The catalyst was durable over a wide pH range. Moreover, the FE values of 1.3%, 21%, and 18.5% were observed at −0.1 V, −0.2 V, and −0.8 V, respectively. The Ni atom sites were stabilized by their coordination with 3 N atoms. Structural characterization techniques and DFT calculations confirmed that among different Ni-N_x sites, Ni-N_3 was likely a catalytically active site for NRR [108]. Further studies need to be made on the design and synthesis of Ni SACs with other coordination structures and tuning of catalyst-support interaction for the NRR.

3.3.2.5 Mo SACs for NRR

A Mo-based structure is the active core in most natural nitrogenase systems, which opens up the possibility of designing single-atom catalysts for ammonia production.

3.3.2.5.1 Mo-N sites

Mo-N active sites have been of paramount importance for the electro-catalytic reduction of N_2 [109]. A cost-effective catalyst SA-Mo/NPC was synthesized by Han et al. *via* atomic dispersion of Mo single atoms on a N-doped porous carbon substrate for effective NRR (Table 3, entry 15). Due to the high density of the active sites and porous carbon framework, the catalyst afforded a high value of NH_3 yield of 34.0 μg h^{-1} mg_{cat}^{-1} and 31.5 μg h^{-1} mg_{cat}^{-1} in 0.1 M KOH and 0.1 M HCl, respectively. Moreover, appreciably high FE values of 14.6% and 6.8% were achieved at −0.30 V and −0.25 V, respectively. XPS measurements suggested that the valence state of Mo in N-doped porous carbon (NPC) was a 3:1 ratio of Mo^{6+} and Mo^{4+}, respectively. The three-dimensional NPC allowed access to the active sites and enhanced mass transport. (Figure 7a). It was further revealed that when the Mo loading on N-doped porous carbon was improved to 9.5

wt%, NH_3 output was enhanced (Figure 7b). A low Mo loading only results in modest benefits, but a high Mo concentration produced nanoclusters and diminished the number of Mo and N bonds, similarly decreasing the ammonia production rate. Mo and N bonds, for example, were thought to be active in the NRR process [27].

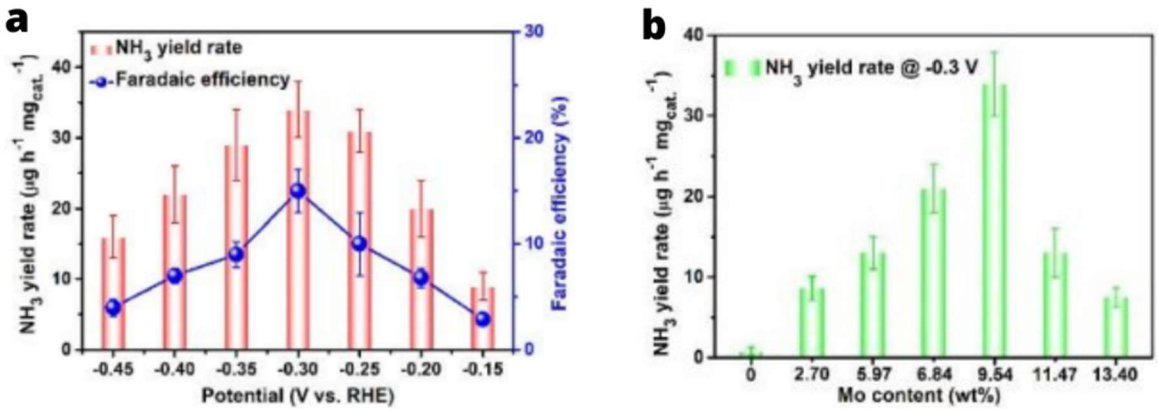

Fig. 7 Electrochemical performances NRR for SA-Mo/NPC in 0.1 M KOH. (a) NH_3 yield rate (red) and FE (blue) at each given potential. (b) NH_3 yield rates of SA-Mo/NPC samples with different Mo loadings. Adapted with permission from Ref. [27], Copyright 2019 WILEY-VCH Verlag GmbH & Co. KGaA, Weinheim.

Recently a more efficient Mo SAs-based electrocatalyst for N_2 reduction has been reported by Zhang et al. to achieve a significantly high FE of 50.2% in an acidic electrolyte under ambient conditions. The Mo/HNG catalyst was obtained by anchoring Mo SAs on carbon fiber paper (Table 3, entry 16). The catalyst achieved an NH_3 yield rate of 3.6 μg h^{-1} mg_{cat}^{-1}. DFT calculations revealed that the edges of the carbon fiber paper being decorated with Mo single atoms as well as the presence of the vacancies of graphene with holes, lowered the overpotential and promoted the NRR [110].

3.3.2.5.2 Mo-C sites

Hui et al. demonstrated an efficient and scalable synthesis of the first selective and bi-functional Mo/GDY electrocatalyst by atomic dispersion of zero-valent Mo SAs up to 7.5% on graphdiyne (GDY) support (Table 3, entry 18). The developed bi-functional catalyst provided promising efficiency and selectivity for NRR and HER in an aqueous solution at ambient conditions. The catalyst achieved an NH_3 yield rate of 145.4 μg h^{-1} mg_{cat}^{-1} and a FE of > 21% in 0.1 M Na_2SO_4. Moreover, the prepared catalyst was stable and could also efficiently catalyze HER in acidic conditions better than commercial 20 wt% Pt/C catalyst [111].

Ma et al. developed Mo SAs-Mo_2C/NCNTs electrocatalysts by dispersing Mo SAs along with Mo carbide particles on N-doped carbon nanotubes (Table 3, entry 19). Individually Mo SAs and Mo_2C exhibited selectivity for HER and NRR, respectively. As predicted by the theoretical calculations, the combination of both Mo SAs and Mo_2C resulted in an integral synergy in the selectivity for HER and NRR in the same catalyst. When the NRR activity of the catalyst developed by dispersion of Mo SAs and Mo_2C on the surface of N-doped carbon nanotubes was evaluated, an efficient NH_3 yield of 16.1 μg h^{-1} cm_{cat}^{-2} at −0.25 V (*vs*. RHE) was obtained. The NH_3 yield rate was four times higher than Mo_2C/NCNTs and 4.5 times higher than Mo SAs/NCNTs. Moreover, the FE of the catalyst was 7.1% which was two times higher than FE of Mo_2C/NCNTs and seven times higher than FE of Mo SAs/NCNTs. The DFT calculations suggested the Mo_2C as the more catalytically active site for NRR compared to the $MoNC_2$ site. The catalyst exhibited stability with unaltered catalytic performance for up to 10 h [112].

3.3.2.6 Mn SACs (Mn-N sites) for NRR

Mn single atom catalyst Mn-N-C SAC was developed by incorporation of Mn single atoms on the ultrathin carbon nanosheets using a folic acid self-assembly strategy (Table 3, entry 17). The developed catalyst exhibited good efficiency and selectivity for the NRR process, imparting an

NH_3 FE of 32.02% and an NH_3 yield of 21.43 μg h^{-1} mg_{cat}^{-1}. The reasonable catalytic activity is attributed to the well-exposed Mn single atoms anchored to 2D conductive carbon substrate. Combined experimental and computational studies suggested that the Mn-N_3 sites were responsible for the catalytic activity. Mn played a distinct role in enhancing N_2 adsorption, activation, and selective reduction following a distal mechanism [113]. Note that Mn SACs for NRR are rarely studied. It is believed that the NRR performance can be further improved by mediating and optimizing the bonding microenvironments of Mn and the properties of supports (e.g., geometric configurations, crystal phases, vacancies, and surface groups).

Table 3 Comparison of the reported SACs' NRR efficiencies

Sr #	SAC	Active site	Catholyte	NH_3 yield rate	NH_3 FE (%)	Potential (V *vs.* RHE)	Ref.
Noble metal-SACs for NRR application							
Noble metal-N coordination							
1	Ru/N-C	Ru-N_4	0.05 M H_2SO_4	120.9 μg h^{-1} mg_{cat}^{-1}	29.6	−0.2	[85]
2	Ru/N-C	Ru-N_x	0.1 M HCl	3665 μg h^{-1} mg_{cat}^{-1}	~7.5	−0.21	
3	Ru@ZrO_2/N-C	Ru-N_x	0.1 M HCl	~1700 μg h^{-1} mg_{cat}^{-1}	21	−0.11	[29]
4	Au_1-C_3N_4	Au-N_3	0.005 M H_2SO_4	1305 μg h^{-1} mg_{cat}^{-1}	11.1	−0.1	[89]
5	Au-NDPCs	Au-N_x	0.1 M HCl	2.32 μg h^{-1} mg_{cat}^{-1}	12.3	−0.2	[90]
Noble metal-O coordination							
6	Ru-SAs/Ti_3C_2O	Ru-O_4	0.1 M HCl	27.56 μg h^{-1} mg_{cat}^{-1}	23.3	−0.2	[87]
Noble metal-C coordination							
7	SA Ru-Mo_2CT_x	Ru-C(O)	0.5 M K_2SO_4	40.57 μg h^{-1} mg_{cat}^{-1}	25.77	−0.3	[88]
Non-noble metal-SACs for NRR application							
Non-noble metal-N coordination							

8	NC-Cu	Cu-N_2	0.1 M KOH 0.1 M HCl	53.3 μg h^{-1} mg_{cat}^{-1} 49.3 μg h^{-1} mg_{cat}^{-1}	13.8 11.7	−0.35 −0.3	[21]
9	ISAS-Fe/N-C	Fe-N_4	0.1 M PBS	62.9 μg h^{-1} mg_{cat}^{-1}	18.6	−0.4	[23]
10	Fe_{SAs}/N-C	Fe-N_4	0.1 M KOH	7.48 μg h^{-1} mg_{cat}^{-1}	56.55	0	[24]
11	Fe/N-C_{NTs}	Fe-N_3	0.1 M KOH	34.83 μg h^{-1} mg_{cat}^{-1}	9.28	−0.2	[25]
12	Fe_1/N-C	Fe-N_4	0.1 M HCl	1.56×10^{11} mol cm^{-2} s^{-1}	4.51	−0.05	[26]
13	Co/N-C	Co-N_x	0.1 M KOH	5.1 μg h^{-1} mg_{cat}^{-1}	10.1	−0.4	[22]
14	Ni−N_x-C	Ni-N_3	0.1 M HCl 0.1 M KOH 0.5 M $LiClO_4$	60 μg h^{-1} mg_{cat}^{-1} 85 μg h^{-1} mg_{cat}^{-1} 115 μg h^{-1} mg_{cat}^{-1}	1.3 21 18.5	−0.1 −0.2 −0.8	[108]
15	SA-Mo/NPC	Mo-N_3	0.1 M KOH 0.1 M HCl	34 μg h^{-1} mg_{cat}^{-1} 31.5 μg h^{-1} mg_{cat}^{-1}	14.6 6.8	−0.3 −0.25	[27]
16	Mo/HNG	Mo-N_x	0.05 M H_2SO_4	3.6 μg h^{-1} mg_{cat}^{-1}	50.2	−0.05	[110]
17	Mn-N-C SACs	Mn-N_3	0.1 M NaOH	21.43 μg h^{-1} mg_{cat}^{-1}	32.02	−0.45	[113]
Non-noble metal-C coordination							
18	Mo^0/GDY	Mo-C_x	0.1 M Na_2SO_4	145.5 μg h^{-1} mg_{cat}^{-1}	>21	-	[111]
19	Mo SAs-Mo_2C/NCNT	Mo-C_x	0.005 M H_2SO_4 + 0.1 M K_2SO_4	16.1 μg h^{-1} cm^{-2}	7.1	−0.25	[112]
Non-noble metal-O coordination							
20	Fe_{SAs}/LCC/CC	Fe-$(O\text{-}C_2)_4$	0.1 M KOH	32.1 μg h^{-1} mg_{cat}^{-1}	29.3	−0.1	[105]
21	Fe_{SAs}/LCC/GC	Fe-$(O\text{-}C_2)_4$	0.1 M KOH	307.7 μg h^{-1} mg_{cat}^{-1} 174.8 μg h^{-1} mg_{cat}^{-1}	51.0 54.1	−0.15 −0.05	
22	Fe/MoS_2	Fe-O_3, Fe-S_1	0.5 K_2SO_4	8.63 μg h^{-1} mg_{cat}^{-1}	18.8	−0.3	[106]

Non-metal SACs show very weak adsorption of protons (H^+). As a result of this, non-metal atoms are more likely to react with N_2 (weak Lewis base) and enhance the nitrogen reduction

reaction. Furthermore, when the NRR activity is tuned by structural deformation, coordinated species attached to the non-metal atoms acts as electron donor and acceptor [114].

Wen et al., for example, used S and boron-doped carbon nanofibers to attain a significant NRR performance [115]. The original sp^2 hybridization and conjugated planar structure may be preserved in the boron-doped graphene skeleton; however, boron and carbon have electronegativities (EN) of 2.04 and 2.55 respectively, and this lower EN value of boron causes a shift in density of electrons from boron to the carbon ring structure. Boron with electron deficient sites promotes N_2 uptake while inhibiting H^+ adsorption.

Yu and colleagues discovered that at −0.5 V (*vs*. RHE), the ammonia production of boron (B)-doped graphene was 9.8 g h^{-1} cm^{-2}, with a FE of 10.8% [116]. Furthermore, DFT studies revealed that BC_3 had the lowest energy barrier for electrocatalytic ammonia production among the various B-doped carbon structures [80]. Liu and colleagues created 21-models incorporating multiple boron states [117] using a single atom of boron adorned on 8 typical 2D materials (Figure 8a). Unlike transition metal *d* orbitals, the boron atom's sp^3 hybrid orbital may receive the lone-pair electrons of N_2, producing B-to-N π back bonding. Single boron atoms supported on Gr and substituted into *h*-MoS_2 showed remarkable selectivity and energy efficiency in the distal route, with comparatively low energy barriers of 0.31 and 0.46 eV, respectively (Figure 8b).

Similarly, when phosphorus (P) (electropositive single atom) is put on a carbon substrate, electronegative carbon atoms are coordinated. These P atoms are transformed into Lewis's acid sites (LAS) and serve as the active center of nitrogen adsorption. Hu and colleagues synthesized a metal-free electrocatalyst which consists of a phosphorus-doped carbon nanotube (PCNTs) for the NRR [24, 118]. By Raman spectroscopy, it was observed that PCNTs had more surface defects than pure CNTs.

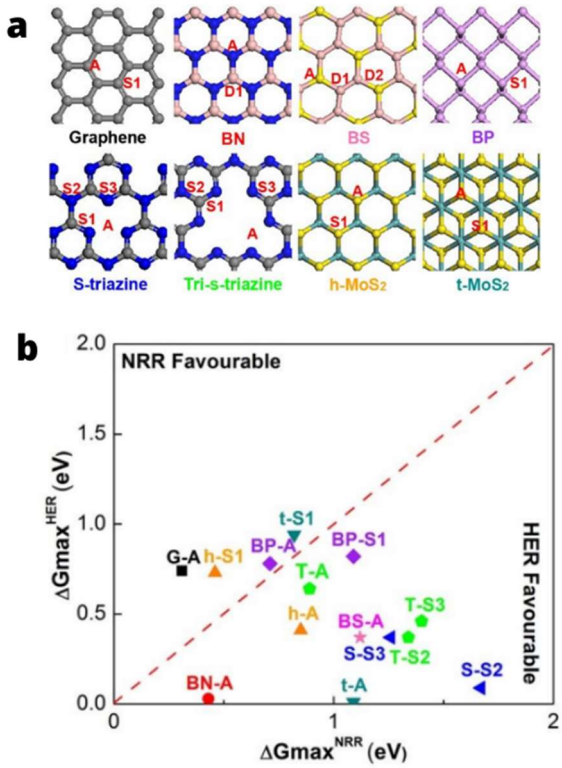

Fig. 8 (a) Proposed 2D materials and potential B-sites. The numbers indicate different bonding environments described in the text. Black, blue, rose, yellow, purple, and cyan spheres represent carbon, nitrogen, boron, sulfur, phosphorus, and molybdenum, respectively. (b) Computational screening of fourteen catalysts combinations (ΔG_{max}^{HER} *vs*. ΔG_{max}^{NRR}). Adapted with permission from Ref. [117], Copyright 2019 American Chemical Society.

Furthermore, pristine CNTs and carbon fiber (bare) produced minimal NH_3 yields as compared to PCNTs which produced up to 24.4 μg h^{-1} mg_{cat}^{-1}. The connection between P-dopant addition and NH_3 production was virtually linear, indicating that the P centers were the actual reactive sites for the nitrogen reduction. According to the Mullikan charge density distribution, P atoms afforded LAS to react with N_2 in PCNTs. And the alternating single and double bonds (π-network) of PCNTs also increased the reduction of nitrogen as compared to P-doped porous carbon nanosheets.

Nonmetallic SACs for NRR are an emerging research area. Mechanistic insights into reaction mechanisms as well as the actual reaction active sites need to be further investigated by combining

theoretical calculations and *in situ* or operando characterizations as well as multiple control experiments.

3.3.3 Theoretical predicted SACs for NRR

3.3.3.1 Pt-based SACs

Although Pt is a very efficient catalytic component in many processes, it has a larger affinity for hydrogen in the electrolyte than it does for nitrogen; as a result, its surface is frequently covered by H, resulting in low electrocatalytic activity for ammonia production in an aqueous environment [119].

Yin and colleagues investigated the potential of single transition metal (TM)/monolayer graphitic carbon nitride (*g*-C_3N_4) (TM = Sc Cu, Mo, Ru, Rh, Pd, Re, Ir, and Pt) as efficient electrochemical NRR SACs in a structured manner [120]. First-principles calculations demonstrated that the experimentally accessible system, platinum-embedded-*g*-C_3N_4 (Pt/*g*-C_3N_4), not only had superior stability and electric conductivity but also had outstanding activity at 25 ºC with a low limiting potential of 0.24 V. The atoms of Pt were tightly anchored to *g*-C_3N_4 to avoid accumulations, resulting in exceptional stability. Furthermore, the preferential adsorption of N_2 over H atoms on Pt/*g*-C_3N_4 allows for excellent HER suppression, resulting in enhanced NRR selectivity. Mechanistic studies revealed that the Pt atom and *g*-C_3N_4 working together addressed the weaker interactions of $*N_2H$ and $*NH_2$, leading to extremely active locations for electrochemical NRR catalysis. The high hydrophobicity of Pt/*g*-C_3N_4 counteracted the fact that Pt preferred to adsorb H rather than N, thereby inhibiting the HER. As a result, Pt/*g*-C_3N_4 demonstrated exceptional NRR activity with a low limiting potential for ammonia synthesis.

3.3.3.2 Co-based SACs for NRR

In general, Co-based catalysts perform well in O_2 and CO_2 reduction reactions [82] because the interaction of cobalt and nitrogen boosts the Co atom's magnetic moment. Because of this structure, Co-based catalysts are catalytically more efficient than standard noble metal catalysts, which plays a crucial role in activating the reactants. To investigate the stability and NRR process of single Co atoms supported on defective N-doped graphene (Co/N_3-Gr), Sardroodi and colleagues used first-principles DFT simulations [121] and determined that Co atoms were tightly bound to the adjacent nitrogen atoms by examining the adsorption energy and formation energy of Co/N_3-Gr. Due to its higher adsorption energy and electron transfer, N_2 was most likely to adhere to the active sites of cobalt (Figure 9a). Because of the reduced overpotential, the Co/N_3-Gr system is predicted to catalyze NRR via an enzymatic process in the aqueous phase (Figure 9b). Co/N_3-Gr needed a greater overpotential for the HER than the NRR (Figure 9c). As a result of the Co atom's strong spin polarization, the non-noble metal Co/N_3-Gr catalyst might be a good electrocatalyst for the NRR.

3.3.3.2 Mo-based SACs for NRR

Wang and colleagues used DFT calculations to examine several SAs on N-doped carbon and discovered that atomically distributed Mo SAC on N-doped carbon showed very good results for NRR to produce NH_3 [49]. Among the studied electrocatalysts, MoN_1C_2 was active for NRR showing an overpotential of 240 mV. The creation of the Mo_1N_3 site and the high stability of the N_2H^* species are responsible for the improved NRR performance. Moreover, Tang and colleagues studied Mo SAs coordinated on boron-CN (Mo-BCN) and observed that NRR was facilitated by using enzymes [122]. This electrocatalyst was able to increase NH_3 production with an overpotential of 420 mV. Song and colleagues investigated the performance of an electrocatalyst

of Mo SAs coordinated on N-doped black phosphorus and observed a very low overpotential of 0.02 V [59].

3.3.3.3 W-based SACs for NRR

At present, atomically distributed tungsten catalysts for the NRR are only being studied theoretically rather than being tested experimentally. Du and coworkers examined NRR performance and processes on a variety of carbon supported-SACs, and discovered that atomic distribution of W-SACs on the graphene had the best results for NRR, with a low onset potential of 0.25 V (*vs*. RHE) [123]. The results showed that the process of N_2 activation for NRR increased when one N-coordination W-SAC anchored on three carbon atoms in the graphene substrate. They also used DFT simulations to investigate the catalytic performance of W-SAC N-doped graphyne for NRR [124]. Theoretical studies revealed that the distal mechanism is advantageous for the NRR, with an onset potential of 0.29 V (*vs*. RHE), which was attributed to the coordination of one W atom with one N atom instead of WN_2 or WN_3. These theoretical investigations pave the way for the experimental fabrication of high-performance atomically distributed W-based NRR catalysts.

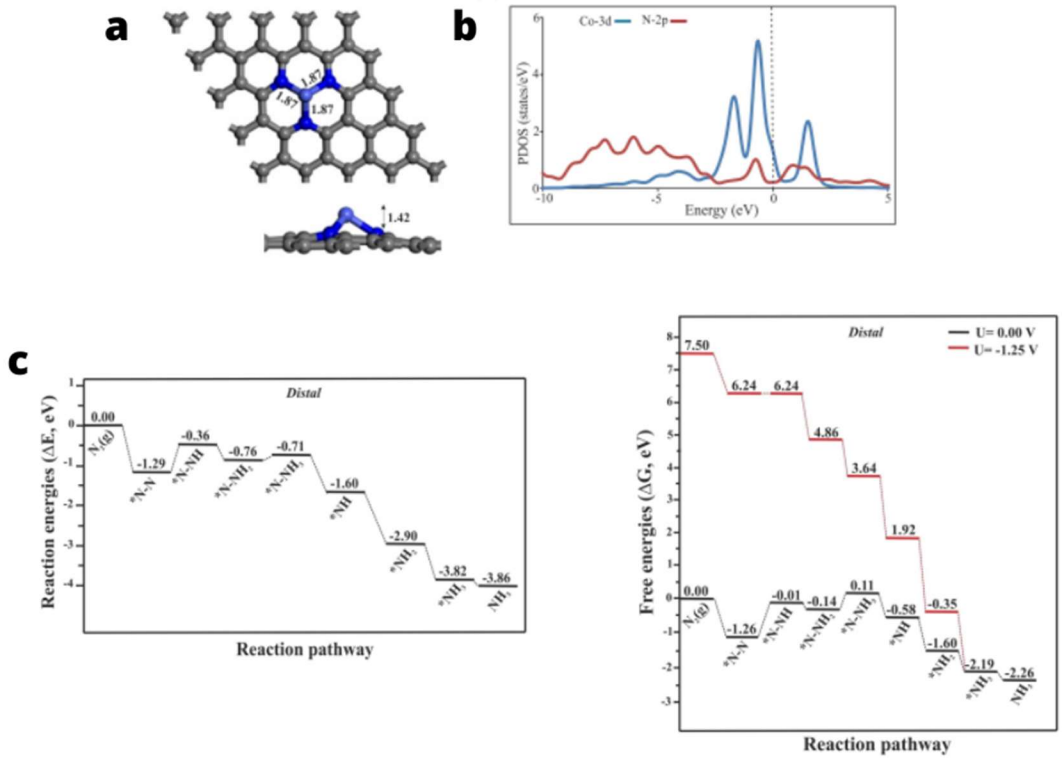

Fig. 6 (a) Top and side views of the optimized structures of Co/N_3-Gr monolayer and (b) partial density of states (PDOS) plot of Co/N_3-Gr monolayer. Fermi level is set to be zero and the bond distance is in Å. (c) Reaction energy (left) and Gibbs free energy (right) diagrams for N_2 reduction reaction on Co/N_3-Gr through distal pathway at zero and applied potentials (limiting potential). Adapted with permission from Ref. [116], Copyright 2019 WILEY-VCH Verlag GmbH & Co. KGaA, Weinheim.

4 Conclusion and future perspectives

SACs are of great interest due to their high catalytic performances, unique atomic structures, and electronic properties. By reduction of the atomic cluster size, the atom utilization efficiencies of the SACs greatly increase. Moreover, the quantum size effect of the coordination of single atoms with N, O, and C plays a significant role in increasing the adsorption and activation of N_2. Judicious theoretical computation could predict the efficiencies and the mechanism of NRR, which help design new and more efficient SACs. Furthermore, advanced characterization techniques such as

XPS, HAADF-STEM, and operando X-ray adsorption (XAS) techniques enable the identification of the presence of single atoms, their coordination, active sites, and the morphologies formed at the surface of the substrate by coordination. Recently several theoretical studies have shown the potential of the noble metal-based SACs for NRR application but experimentally Ru, Au, and Cu SACs have only been reported. Non-noble metals-based SACs offer cheap and durable alternatives with promising catalytic activity and FE towards NH_3 formation. However, till now the NRR performances of nonmetal SACs have only been investigated through theoretical predictions. Despite reasonable efficiencies, their selectivity and stability still need to be improved further to realize the N_2 reduction to meet up the demands of industrial-scale applications.

Precise, reliable, and repeatable methods for ex-situ and in-situ detection and quantification of NH_3 are still required [125−127]. Equally importantly, exogenous nitrogen contaminants should be avoided prior to and during the NRR. To this end, use of N_2 and Ar with purity over 99.999% are preferred in the NRR. In addition, the N_2 reactant, Ar gas, electrolytes, and membranes should be cleaned before NRR. Furthermore, $^{15}N_2$ isotopic labeling is strongly suggested to be performed to confirm the origin of the evolved NH_3, especially for electrocatalysts that contain nitrogen compositions or are synthesized from nitrogen-containing precursors or solvents.

N_2 electrochemical reduction is a complex process, and its efficiency depends not only on the optimal conditions and electrolytes but also on the configuration and interactions of the catalyst with support. The optimum conditions, yield, and efficiency of the NRR strongly relate to the catalytic active site (depending on catalyst and support), and the mechanism of the NRR process. The competitive adsorption of hydrogen on the active site is potential dependent. Hence at the negative potentials, the hydrogen-occupied catalytic surface leads to low efficiency of the NRR [126, 128]. Design of electrocatalysts that can positively shift the overpotential would weaken the

HER. Both more efficient single atoms, as well as efficient supports, are required to achieve the desired stability and selectivity. Use of different fabrication techniques as well as defect engineering strategies to regulate the electrical conductivities and catalytic activities, such as to suppress the HER, should be explored. The proton transfer rates should be limited to control the outcome of the electrocatalytic reduction process. This can be achieved by decreasing proton transfer rate either via reducing the concentration of protons in the electrolyte or increasing the barrier to the catalyst surface. Alternatively, introduction of a H^+-coupled e^- transfer mediator enables a spatial and electronical separation of H^+ and e^- relays, thus mitigating the HER. The modulation of the proton transfer rate can be also accomplished by tuning the chemical affinity of the catalytic surface through material engineering. Using a hydrophobic (proton deficient) support offers an effective methodology to limit the accessibility of protons to the catalytic site [129, 130]. Five times increase in the FE was observed by catalyst supported on a hydrophobic substrate [131]. Design and construction of dual-metallic single atom catalysts provides another route to improve catalytic efficiency and stability as opposed to uni-metallic single atom catalysts, owing to the strong bonding between the dual metal single atoms and the prominent interaction of the dual sites with the support [132−134]. Moreover, the peculiar electronic and geometric synergy of dual metallic single atom catalysts favors high NRR selectivity toward NH_3 [135].

Further, there is a tremendous increase in theoretical calculations reporting better efficiencies of SACs for NRR application but unfortunately, only a few experimental studies have been realized to validate the predicted efficiencies and to obtain actual experimental efficiencies by the synthesis of the predicted SACs. There is great room for experimental studies to synthesize and explore the potential of NRR. We strongly believe that SACs have great potential to realize an effective method to produce NH_3, a clean energy source expected to have the potential to replace

fossil fuels in the future. This review provides useful insight to promote continued research in this field for the electrocatalytic performance of SACs to convert N_2 to NH_3 efficiently.

It is noted that the NH_3 yield rate and FE via direct electrochemical NRR are still rather low, far less than the commercial desired production rate of 9.3×10^{-7} mol cm^{-2} s^{-1}. To solve this issue, a promising route for ambient and large-scale ammonia electrosynthesis from nitrogen is the lithium-mediated process using gas diffusion electrodes to minimize the migration distance of N_2 through the electrolyte to react at the catalyst surface. Alternatively, the application of bioelectrocatalysis in combination with single-atom electrocatalysis allows for maximization of active sites, enhancement of electron transfer, suppression of the parasitic HER, and creation of a tandem catalytic system, thereby greatly boosting NH_3 production. More future research efforts are suggested to focus in this regard.

Acknowledgments

This work was supported by the National Natural Science Foundation of China (no. 21972010) and Beijing Natural Science Foundation (no. 2192039).

Declarations

Conflict of interests

The authors declare that they have no conflict of interest.

References

[1] Wan J, Zheng J, Zhang H, Wu A, Li X. Single atom catalysis for electrocatalytic ammonia synthesis. Catal Sci Technol. 2022;12(1):38. https://doi.org/10.1039/D1CY01442K.

[2] Hao Q, Liu C, Jia G, Wang Y, Arandiyan H, Wei W, Ni BJ. Catalytic reduction of nitrogen to produce ammonia by bismuth-based catalysts: state of the art and future prospects. Mater Horiz. 2020;7(4):1014. https://doi.org/10.1039/C9MH01668F.

[3] Schlögl R. Catalytic synthesis of ammonia — a "Never-Ending Story"? Angew Chem Int Ed. 2003;42(18):2004. https://doi.org/10.1002/anie.200301553.

[4] Chen GF, Ren S, Zhang L, Cheng H, Luo Y, Zhu K, Ding LX, Wang H. Nitrogen reduction reactions: advances in electrocatalytic N_2 reduction — strategies to tackle the selectivity challenge. Small Methods. 2019;3(6):1970016. https://doi.org/10.1002/smtd.20.

[5] Shen H, Yang, M, Hao, L, Wang J, Strunk J, Sun Z. Photocatalytic nitrogen reduction to ammonia: insights into the role of defect engineering in photocatalysts. Nano Res. 2022, 15, 2773. https://doi.org/10.1007/s12274-021-3725-0.

[6] Hu P, Huang Z, Amghouz Z, Makkee M, Xu F, Kapteijn F, Dikhtiarenko A, Chen Y, Gu X, Tang XF. Electronic metal-support interactions in single-atom catalysts. Angew Chem. 2014;126(13):3486. https://doi.org/10.1002/anie.201309248.

[7] Liu JD, Wei ZX, Dou YH, Feng YZ, Ma JM. Ru-doped phosphorene for electrochemical ammonia synthesis. Rare Metals. 2020;39(8):874-880. https://doi.org/10.1007/s12598-020-01451-z.

[8] Légaré MA, Bélanger-Chabot G, Dewhurst RD, Welz E, Krummenacher I, Engels B, Braunschweig H. Nitrogen fixation and reduction at boron. Science. 2018;359(6378):896. https://doi.org/10.1126/science.aaq1684.

[9] McCoy D, Feo T, Harvey T, Prum R. Structural absorption by barbule microstructures of super black bird of paradise feathers. Nat Commun. 2018;9:1. https://doi.org/10.1038/s41467-017-02088-w.

[10] Tang C, Qiao SZ. How to explore ambient electrocatalytic nitrogen reduction reliably and insightfully. Chem Soc Rev. 2019;48(12):3166. https://doi.org/10.1039/C9CS00280D.

[11] Chen Y, Wang L, Yao Z, Hao L, Tan X, Masa J, Robertson AW, Sun, Z. Tuning the coordination structure of single atoms and their interaction with the support for carbon dioxide electroreduction. Acta Phys Chim Sin. 2022;38(11):2206020. https://doi.org/10.3866/PKU.WHXB202207024.

[12] Gao Y, Yang Y, Hao L, Hong S, Tan X, Wu TS, Sun Z. Single Nb atom modified anatase TiO_2(110) for efficient electrocatalytic nitrogen reduction reaction. Chem Catal. 2022. https://doi.org/10.1016/j.checat.2022.06.010.

[13] Jiang Y, Sung Y, Choi C, Joo Bang G, Hong S, Tan X, Wu TS, Soo YL, Xiong P, Li M-J, Hao L, Jung Y. Sun Z. Single-atom molybdenum-N_3 sites for selective hydrogenation of CO_2 to CO. Angew Chem Int Ed. 2022;61:e202203836. https://doi.org/10.1002/anie.202203836.

[14] Jia, M, Fan, Q, Liu, S, Qiu, J, Sun Z. Single-atom catalysis for electrochemical CO_2 reduction. Curr Opin Green Sustain Chem. 2019:16:1−6. https://doi.org/10.1016/j.cogsc.2018.11.002.

[15] Yao Y, Wang J, Shahid UB, Gu M, Wang H, Li H, Shao MJ. Electrochemical synthesis of ammonia from nitrogen under mild conditions: current status and challenges. Electrochem Energy Rev. 2020;3(2):239. https://doi.org/10.1007/s41918-019-00061-3.

[16] Shi L, Yin Y, Wang S, Sun H. Rational catalyst design for N_2 reduction under ambient conditions: strategies toward enhanced conversion efficiency. ACS Catal. 2020;10(12):6870. https://doi.org/10.1021/acscatal.0c01081.

[17] Li M, Huang H, Low J, Gao C, Long R, Xiong YJ. Recent progress on electrocatalyst and photocatalyst design for nitrogen reduction. Small Methods. 2019;3(6):1800388. https://doi.org/10.1002/smtd.201800388.

[18] Li Y, Zhang Q, Li C, Fan HN, Luo WB, Liu HK, & Dou SX. Atomically dispersed metal dimer species with selective catalytic activity for nitrogen electrochemical reduction. J Mater Chem A. 2019;7(39): 22242−22247. https://doi.org/10.1039/C9TA07845B

[19] Lazouski N, Chung M, Williams K, Gala ML, Manthiram K. Non-aqueous gas diffusion electrodes for rapid ammonia synthesis from nitrogen and water-splitting-derived hydrogen. Nat Catal. 2020;3(5):463. https://doi.org/10.1038/s41929-020-0455-8.

[20] Liu Y, Xu Q, Fan X, Quan X, Su Y, Chen S, Yu H, Cai Z. Electrochemical reduction of N_2 to ammonia on Co single atom embedded N-doped porous carbon under ambient conditions. J Mater Chem A. 2019;7(46):26358. https://doi.org/10.1039/C9TA10382A.

[21] Zang W, Yang T, Zou H, Xi S, Zhang H, Liu X, Kou Z, Du Y, Feng YP, Shen L. Copper single atoms anchored in porous nitrogen-doped carbon as efficient pH-universal catalysts for the nitrogen reduction reaction. ACS Catal. 2019;9(11):10166. https://doi.org/10.1021/acscatal.9b02944.

[22] Gao Y, Han Z, Hong S, Wu T, Li X, Qiu J, Sun Z. ZIF-67-derived cobalt/nitrogen-doped carbon composites for efficient electrocatalytic N_2 reduction. ACS Appl Energy Mater. 2019;2(8):6071. https://doi.org/10.1021/acsaem.9b01135.

[23] Lü F, Zhao S, Guo R, He J, Peng X, Bao H, Fu J, Han L, Qi G, Luo J. Nitrogen-coordinated single Fe sites for efficient electrocatalytic N_2 fixation in neutral media. Nano Energy. 2019;61:420. https://doi.org/10.1016/j.nanoen.2019.04.092.

[24] Wang M, Liu S, Qian T, Liu J, Zhou J, Ji H, Xiong J, Zhong J, Yan C. Over 56.55% Faradaic efficiency of ambient ammonia synthesis enabled by positively shifting the reaction potential. Nat Commun. 2019;10(1):341. https://doi.org/10.1038/s41467-018-08120-x

[25] Wang Y, Cui X, Zhao J, Jia G, Gu L, Zhang Q, Meng L, Shi Z, Zheng L, Wang C. Rational design of Fe-N/C hybrid for enhanced nitrogen reduction electrocatalysis under ambient conditions in aqueous solution. ACS Catal. 2018;9(1):336. https://doi.org/10.1021/acscatal.8b03802.

[26] Zhang R, Jiao L, Yang W, Wan G, Jiang H-L. Single-atom catalysts templated by metal-organic frameworks for electrochemical nitrogen reduction. J Mater Chem A. 2019;7(46):26371. https://doi.org/10.1039/C9TA10206J.

[27] Han L, Liu X, Chen J, Lin R, Liu H, Lü F, Bak S, Liang Z, Zhao S, Stavitski EJ. Atomically dispersed molybdenum catalysts for efficient ambient nitrogen fixation. Angew Chem Int Ed. 2019;58(8):2321. https://doi.org/10.1002/anie.201811728.

[28] Yuan LP, Wu ZY, Jiang WJ, Tang T, Niu S, Hu JS. Phosphorus-doping activates carbon nanotubes for efficient electroreduction of nitrogen to ammonia. Nano Res. 2020;13(5):1376. https://doi.org/10.1007/s12274-020-2637-8.

[29] Tao H, Choi C, Ding L-X, Jiang Z, Han Z, Jia M, Fan Q, Gao Y, Wang H, Robertson A. Nitrogen fixation by Ru single-atom electrocatalytic reduction. Chem. 2019;5(1):204. https://doi.org/10.1016/j.chempr.2018.10.007.

[30] Yu B, Li H, White J, Donne S, Yi J, Xi S, Fu Y, Henkelman G, Yu H, Chen ZJ. Tuning the catalytic preference of ruthenium catalysts for nitrogen reduction by atomic dispersion. Adv Funct Mater. 2019;30(6):1905665. https://doi.org/10.1002/adfm.201905665.

[31] Liu J, Kong X, Zheng L, Guo X, Liu X, Shui J. Rare earth single-atom catalysts for nitrogen and carbon dioxide reduction. ACS Nano. 2020;14(1):1093. https://doi.org/10.1021/acsnano.9b08835.

[32] Wang Q, Zheng G, Hao S, Liu X, Zheng J, Wang Y, Su Z, Xu N, He Y, Lei L, Zhang X. Au_1Co_1 alloy supported on graphene oxide with enhanced performance for ambient electrolysis of nitrogen to ammonia. ACS Sustain Chem Eng. 2020;8(1):44-9. https://doi.org/10.1021/acssuschemeng.9b06827.

[33] Zhang L, Ji X, Ren X, Luo Y, Shi X, Asiri AM, Zheng B, Sun X. Correction to "Efficient electrochemical N_2 reduction to NH_3 on MoN nanosheets array under ambient conditions". ACS Sustain Chem Eng. 2018;7(1):1807. https://doi.org/10.1021/acssuschemeng.8b05648.

[34] Wu X, Wang Z, Han Y, Zhang D, Wang M, Li H, Zhao H, Pan Y, Lai J, Wang L. Chemically coupled NiCoS/C nanocages as efficient electrocatalysts for nitrogen reduction reactions. J Mater Chem A. 2020;8(2):543. https://doi.org/10.1039/C9TA10142J.

[35] Liu Y, Huang L, Zhu X, Fang Y, Dong S. Coupling Cu with Au for enhanced electrocatalytic activity of nitrogen reduction reaction. Nanoscale. 2020;12(3):1811. https://doi.org/10.1039/C9NR08788E.

[36] Liu A, Gao M, Ren X, Meng F, Yang Y, Yang Q, Guan W, Gao L, Liang X, Ma T. A two-dimensional Ru@MXene catalyst for highly selective ambient electrocatalytic nitrogen reduction. Nanoscale. 2020;12(20):10933. https://doi.org/10.1039/D0NR00788A.

[37] Zhao R, Liu C, Zhang X, Zhu X, Wei P, Ji L, Guo Y, Gao S, Luo Y, Wang Z. An ultrasmall Ru_2P nanoparticles-reduced graphene oxide hybrid: an efficient electrocatalyst for NH_3 synthesis under ambient conditions. J Mater Chem A. 2020;8(1):77. https://doi.org/10.1039/C9TA10346E.

[38] Li L, Tang C, Xia B, Jin H, Zheng Y, Qiao S. Two-dimensional mosaic bismuth nanosheets for highly selective ambient electrocatalytic nitrogen reduction. ACS Catal. 2019;9(4):2902. https://doi.org/10.1021/acscatal.9b00366.

[39] Zhang X, Wu T, Wang H, Zhao R, Chen H, Wang T, Wei P, Luo Y, Zhang Y, Sun X. Boron nanosheet: an elemental two-dimensional (2D) material for ambient electrocatalytic N_2-to-NH_3 fixation in neutral media. ACS Catal. 2019;9(5):4609. https://doi.org/10.1021/acscatal.8b05134.

[40] Wang Z, Gong F, Zhang L, Wang R, Ji L, Liu Q, Luo Y, Guo H, Li Y, Gao P. Electrocatalytic hydrogenation of N_2 to NH_3 by MnO: experimental and theoretical investigations. Adv Sci. 2018;6(1):1801182. https://doi.org/10.1002/advs.201801182.

[41] Zhang L, Ding L, Chen G, Yang X, Wang H. Ammonia synthesis under ambient conditions: selective electroreduction of dinitrogen to ammonia on black phosphorus nanosheets. Angew Chem. 2019;131(9):2638. https://doi.org/10.1002/anie.201813174.

[42] Zhao J, Wang B, Zhou Q, Wang H, Li X, Chen H, Wei Q., Wu D, Luo Y, You JJ. Efficient electrohydrogenation of N_2 to NH_3 by oxidized carbon nanotubes under ambient conditions. Chem Comm. 2019;55(34):4997. https://doi.org/10.1039/C9CC00726A.

[43] Zhu X, Wu T, Ji L, Li C, Wang T, Wen S, Gao S, Shi X, Luo Y, Peng Q. Ambient electrohydrogenation of N_2 for NH_3 synthesis on non-metal boron phosphide nanoparticles: the

critical role of P in boosting the catalytic activity. J Mater Chem A. 2019;7(27):16117. https://doi.org/10.1039/C9TA05016G.

[44] Zhang G, Ji Q, Zhang K, Chen Y, Li Z, Liu H, Li J, Qu J. Triggering surface oxygen vacancies on atomic layered molybdenum dioxide for a low energy consumption path toward nitrogen fixation. Nano Energy. 2019;59:10. https://doi.org/10.1016/j.nanoen.2019.02.028.

[45] Guo W, Zhang K, Liang Z, Zou R, Xu Q. Electrochemical nitrogen fixation and utilization: theories, advanced catalyst materials and system design. Chem Soc Rev. 2019;48(24):5658. https://doi.org/10.1039/C9CS00159J.

[46] Yan X, Liu D, Cao H, Hou F, Liang J, Dou SX. Nitrogen reduction to ammonia on atomic-scale active sites under mild conditions. Small Methods. 2019;3(9):1800501. https://doi.org/10.1002/smtd.201800501.

[47] Li X-F, Li Q-K, Cheng J, Liu L, Yan Q, Wu Y, Zhang XH, Wang ZY, Qiu Q, Luo Y. Conversion of dinitrogen to ammonia by FeN_3-embedded graphene. J Am Chem Soc. 2016;138(28):8706. https://doi.org/10.1021/jacs.6b04778.

[48] Shen H, Choi C, Masa J, Li X, Qiu J, Jung Y, Sun Z. Electrochemical ammonia synthesis: mechanistic understanding and catalyst design. Chem. 2021;7(7):1708. https://doi.org/10.1016/j.chempr.2021.01.009.

[49] Ling C, Bai X, Ouyang Y, Du A, Wang J. Single molybdenum atom anchored on N-doped carbon as a promising electrocatalyst for nitrogen reduction into ammonia at ambient conditions. J Phys Chem C. 2018;122(25):16842. https://doi.org/10.1021/acs.jpcc.8b05257.

[50] van der Ham CJM, Koper MTM, Hetterscheid DGH. Challenges in reduction of dinitrogen by proton and electron transfer. Chem Soc Rev. 2014;43(15):5183. https://doi.org/10.1039/C4CS00085D.

[51]. Nishibayashi Y. Recent progress in transition-metal-catalyzed reduction of molecular dinitrogen under ambient reaction conditions. Inorg Chem. 2015;54(19):9234. https://doi.org/10.1021/acs.inorgchem.5b00881.

[52] Singh AR, Rohr BA, Schwalbe JA, Cargnello M, Chan K, Jaramillo TF, Chorkendorff I, Nørskov JK. Electrochemical ammonia synthesis-the selectivity challenge. ACS Catal. 2016;7(1):706. https://doi.org/10.1021/acscatal.6b03035.

[53] Wang S, Ichihara F, Pang H, Chen H, Ye J. Nitrogen fixation reaction derived from nanostructured catalytic materials. Adv Funct Mater. 2018;28(50):1803309. https://doi.org/10.1002/adfm.201803309.

[54] Zhou F, Azofra LM, Ali M, Kar M, Simonov AN, McDonnell-Worth C, Sun C, Zhang X, MacFarlane DR. Electro-synthesis of ammonia from nitrogen at ambient temperature and pressure in ionic liquids. Energy Environ Sci. 2017;10(12):2516. https://doi.org/10.1039/C7EE02716H.

[55] Suryanto BHR, Kang CSM, Wang D, Xiao C, Zhou F, Azofra LM, Cavallo L, Zhang X, MacFarlane D. Rational electrode-electrolyte design for efficient ammonia electrosynthesis under ambient conditions. ACS Energy Lett. 2018;3(6):1219. https://doi.org/10.1021/acsenergylett.8b00487.

[56] Zhang L, Mallikarjun Sharada S, Singh AR, Rohr BA, Su Y, Qiao L, Nørskov J. A theoretical study of the effect of a non-aqueous proton donor on electrochemical ammonia synthesis. Phys Chem Chem Phys. 2018;20(7):4982. https://doi.org/10.1039/C7CP05484J.

[57] Koh CSL, Lee HK, Fan Sim HY, Han X, Phan-Quang GC, Ling XY. Turning water from a hindrance to the promotor of preferential electrochemical nitrogen reduction. Chem Mater. 2020;32(4):1674. https://doi.org/10.1021/acs.chemmater.9b05313.

[58] Zheng J, Lyu Y, Qiao M, Wang R, Zhou Y, Li H, Chen C, Li Y, Zhou H, Wang S. Photoelectrochemical synthesis of ammonia on the aerophilic-hydrophilic heterostructure with 37.8% efficiency. Chem. 2019;5(3):617. https://doi.org/10.1016/j.chempr.2018.12.003.

[59] Ou P, Zhou X, Meng F, Chen C, Chen Y, Song J. Single molybdenum center supported on N-doped black phosphorus as an efficient electrocatalyst for nitrogen fixation. Nanoscale. 2019;11(28):13600. https://doi.org/10.1039/C9NR02586C.

[60] Medford AJ, Vojvodic A, Hummelshøj JS, Voss J, Abild-Pedersen F, Studt F, Bligaard T, Nilsson A, Nørskov J. From the Sabatier principle to a predictive theory of transition-metal heterogeneous catalysis. J Catal. 2015;328:36. https://doi.org/10.1016/j.jcat.2014.12.033.

[61] Montoya JH, Tsai C, Vojvodic A, Nørskov JK. The challenge of electrochemical ammonia synthesis: a new perspective on the role of nitrogen scaling relations. ChemSusChem. 2015;8(13):2180. https://doi.org/10.1002/cssc.201500322.

[62] Stamenkovic VR, Mun BS, Arenz M, Mayrhofer KJJ, Lucas CA, Wang G, Ross PN, Markovic N. Trends in electrocatalysis on extended and nanoscale Pt-bimetallic alloy surfaces. Nat Mater. 2007;6(3):241. https://doi.org/10.1038/nmat1840.

[63] Choi C, Back S, Kim N-Y, Lim J, Kim Y-H, Jung Y. Suppression of hydrogen evolution reaction in electrochemical N_2 reduction using single-atom catalysts: a computational guideline. ACS Catal. 2018;8(8):7517. https://doi.org/10.1021/acscatal.8b00905.

[64] Zhu C, Fu S, Shi Q, Du D, Lin Y. Single-atom electrocatalysts. Angew Chem Int Ed. 2017;56(45):13944. https://doi.org/10.1039/D0RA08223F.

[65] Liu P, Zhao Y, Qin R, Mo S, Chen G, Gu L, Chevrier DM, Zhang P, Guo Q, Zang D. Photochemical route for synthesizing atomically dispersed palladium catalysts. Science. 2016;352(6287):797. https://doi.org/10.1126/science.aaf5251.

[66] Thomas JM. The concept, reality and utility of single-site heterogeneous catalysts (SSHCs). Phys Chem Chem Phys. 2014;16(17):7647. https://doi.org/10.1039/C4CP00513A.

[67] O'Neill BJ, Jackson DHK, Lee J, Canlas C, Stair PC, Marshall CL, Elam J, Kuech T, Dumesic J. Huber G. Catalyst design with atomic layer deposition. ACS Catal. 2015;5(3):1804. https://doi.org/10.1021/cs501862h.

[68] Mohanty B, Jena BK, Basu S. Single atom on the 2D matrix: an emerging electrocatalyst for energy applications. ACS Omega. 2020;5(1):1287. https://doi.org/10.1021/acsomega.9b03515.

[69] Sun S, Zhang G, Gauquelin N, Chen N, Zhou J, Yang S, Chen W, Meng X, Geng D, Banis M. Single-atom catalysis using Pt/graphene achieved through atomic layer deposition. Sci Rep. 2013;3(1). https://doi.org/10.1038/srep01775.

[70] Piernavieja-Hermida M, Lu Z, White A, Low K-B, Wu T, Elam JW, Wu Z, Lei Y. Towards ALD thin film stabilized single-atom Pd_1 catalysts. Nanoscale. 2016;8(33):15348. https://doi.org/10.1039/C6NR04403D.

[71] Fei H, Dong J, Feng Y, Allen CS, Wan C, Volosskiy B, Li M, Zhao Z, Wang Y. Sun H. General synthesis and definitive structural identification of MN_4C_4 single-atom catalysts with tunable electrocatalytic activities. Nat Catal. 2018;1(1):63. https://doi.org/10.1038/s41929-017-0008-y.

[72] Xue Y, Huang B, Yi Y, Guo Y, Zuo Z, Li Y, Jia Z, Liu H, Li Y. Anchoring zero valence single atoms of nickel and iron on graphdiyne for hydrogen evolution. Nat Commun. 2018;9(1):1460. https://doi.org/10.1038/s41467-018-03896-4.

[73] Zhang Z, Feng C, Liu C, Zuo M, Qin L, Yan X, Xing Y, Li H, Si R, Zhou S. Electrochemical deposition as a universal route for fabricating single-atom catalysts. Nat Commun. 2020;11(1):1215. https://doi.org/10.1038/s41467-020-14917-6.

[74] Choi CH, Kim M, Kwon HC, Cho SJ, Yun S, Kim HT, Mayrhofer KJ, Kim H, Choi MJ. Tuning selectivity of electrochemical reactions by atomically dispersed platinum catalyst. Nat Commun. 2016;7(1):10922. https://doi.org/10.1038/ncomms10922.

[75] Kwak DH, Han SB, Lee YW, Park HS, Choi IA, Ma KB, Kim MC, Kim SJ, Kim DH, Sohn JI. Fe/N/S-doped mesoporous carbon nanostructures as electrocatalysts for oxygen reduction reaction in acid medium. Appl Catal B Environ. 2017;203:889. https://doi.org/10.1016/j.apcatb.2016.10.084.

[76] Hu K, Tao L, Liu D, Huo J, Wang S. Sulfur-doped Fe/N/C nanosheets as highly efficient electrocatalysts for oxygen reduction reaction. ACS Appl Mater Interfaces. 2016;8(30):19379. https://doi.org/10.1021/acsami.6b02078.

[77] Wang XX, Cullen DA, Pan Y, Hwang S, Wang M, Feng Z, Wang J, Engelhard MH, Zhang H, He Y. Nitrogen-coordinated single cobalt atom catalysts for oxygen reduction in proton exchange membrane fuel cells. Adv Mater. 2018;30(11):1706758. https://doi.org/10.1002/adma.201706758.

[78] Li JC, Wei Z, Liu D, Du D, Lin Y, Shao M. Dispersive single-atom metals anchored on functionalized nanocarbons for electrochemical reactions. Top Curr Chem. 2019;377. https://doi.org/10.1007/s41061-018-0229-9.

[79] Peng Y, Lu B, Chen S. Carbon-supported single atom catalysts for electrochemical energy conversion and storage. Adv Mater. 2018;30(48):1801995. https://doi.org/10.1002/adma.201801995.

[80] Yin P, Yao T, Wu Y, Zheng L, Lin Y, Liu W, Ju H, Zhu J, Hong X, Deng Z. Single atoms with precise N-coordination as superior oxygen reduction reaction catalysts. Angew Chem. 2016;128(36):10958. https://doi.org/10.1002/anie.201604802.

[81] Zhang C, Sha J, Fei H, Liu M, Yazdi S, Zhang J, Zhong Q, Zou X, Zhao N, Yu H. Single-atomic ruthenium catalytic sites on nitrogen-doped graphene for oxygen reduction reaction in acidic medium. ACS Nano. 2017;11(7):6930–41. https://doi.org/10.1021/acsnano.7b02148.

[82] Fei H, Dong J, Arellano-Jiménez MJ, Ye G, Dong Kim N, Samuel ELG, Peng Z, Zhu Z, Qin F, Bao J. Atomic cobalt on nitrogen-doped graphene for hydrogen generation. Nat Commun. 2015;6(1):8668. https://doi.org/10.1038/ncomms9668.

[83] Cui L, Cui L, Li Z, Zhang J, Wang H, Lu S, Xiang Y. A copper single-atom catalyst towards efficient and durable oxygen reduction for fuel cells. J Mater Chem. A. 2019;7(28):16690–5. https://doi.org/10.1039/C9TA03518D.

[84] Li X, Yang X, Huang Y, Zhang T, Liu B. Supported noble-metal single atoms for heterogeneous catalysis. Adv Mater. 2019;31(50):1902031. https://doi.org/10.1002/adma.201902031.

[85] Geng Z, Liu Y, Kong X, Li P, Li K, Liu Z, Du J., Shu M, Si R, Zeng J. Achieving a record-high yield rate of 120.9 μg_{NH3} $mg_{cat.}^{-1}$ h^{-1} for N_2 electrochemical reduction over Ru single-atom catalysts. Adv Mater. 2018;30(40):1803498. https://doi.org/10.1002/adma.201803498.

[86] Yang J, Li W. Wang D, Li Y. Electronic metal-support interaction of single-atom catalysts and applications in electrocatalysis. Adv Mater. 2020;32(49):2003300. https://doi.org/10.1002/adma.202003300.

[87] Chen G, Ding M, Zhang K, Shen Z, Wang Y, Ma J, Wang A, Li Y, Xu H. Single-atomic ruthenium active sites on Ti_3C_2 MXene with oxygen-terminated surface synchronize enhanced activity and selectivity for electrocatalytic nitrogen reduction to ammonia. ChemSusChem. 2022;15(3):e202102352. https://doi.org/10.1002/cssc.202102352.

[88] Peng W, Luo M, Xu X, Jiang K, Peng M, Chen D, Chan TS, Tan Y. Spontaneous atomic ruthenium doping in Mo_2CT_X MXene defects enhances electrocatalytic activity for the nitrogen

reduction reaction. Adv Energy Mater. 2020;10(25):2001364. https://doi.org/10.1002/aenm.202001364.

[89] Wang X, Wang W, Qiao M, Wu G, Chen W, Yuan T, Xu Q, Chen M, Zhang Y, Wang X. Atomically dispersed Au_1 catalyst towards efficient electrochemical synthesis of ammonia. Sci Bull. 2018;63(19):1246. https://doi.org/10.1016/j.scib.2018.07.005.

[90] Qin Q, Heil T, Antonietti M, Oschatz M. Single-site gold catalysts on hierarchical N-doped porous noble carbon for enhanced electrochemical reduction of nitrogen. Small Methods. 2018;2(12):1800202. https://doi.org/10.1002/smtd.201800202.

[91] Guo C, Ran J, Vasileff A, Qiao SZ. Rational design of electrocatalysts and photo(electro)catalysts for nitrogen reduction to ammonia (NH_3) under ambient conditions. Energy Environ Sci. 2018;11(1):45. https://doi.org/10.1039/C7EE02220D.

[92] Bao D, Zhang Q, Meng F-L, Zhong HX, Shi MM, Zhang Y, Yan JM, Jiang Q, Zhang X. Electrochemical reduction of N_2 under ambient conditions for artificial N_2 fixation and renewable energy storage using N_2/NH_3 cycle. Adv Mater. 2016;29(3):1604799. https://doi.org/10.1002/adma.201604799.

[93] Shi MM, Bao D, Wulan BR, Li YH, Zhang YF, Yan JM, Jiang Q. Au sub-nanoclusters on TiO_2 toward highly efficient and selective electrocatalyst for N_2 conversion to NH_3 at ambient conditions. Adv Mater. 2017;29(17):1606550. https://doi.org/10.1002/adma.201606550.

[94] Zhao Y, Shi R, Bian X, Zhou C, Zhao Y, Zhang S, Wu F, Waterhouse GI, Wu LZ, Tung C. Ammonia detection methods in photocatalytic and electrocatalytic experiments: how to improve

the reliability of NH_3 production rates? Adv Sci. 2019;6(8):1802109. https://doi.org/10.1002/advs.201802109.

[95] Chen G, Ren S, Zhang L, Cheng H, Luo Y, Zhu K, Ding LX, Wang H. Advances in electrocatalytic N_2 reduction—strategies to tackle the selectivity challenge. Small Methods. 2018;3(6):1800337. https://doi.org/10.1002/smtd.201800337.

[96] Qu Y, Li Z, Chen W, Lin Y, Yuan T, Yang Z, Zhao C, Wang J, Zhao C, Wang X. Direct transformation of bulk copper into copper single sites via emitting and trapping of atoms. Nat Catal. 2018;1(10):781. https://doi.org/10.1038/s41929-018-0146-x.

[97] Jin Z, Li P, Fang Z, Yu G. Emerging electrochemical techniques for probing site behavior in single-atom electrocatalysts. Acc Chem Res. 2022;55(5):759. https://doi.org/10.1021/acs.accounts.1c00785.

[98] Wang Y, Chen Z, Han P, Du Y, Gu Z, Xu X, Zheng G. Single-atomic Cu with multiple oxygen vacancies on ceria for electrocatalytic CO_2 reduction to CH_4. ACS Catal. 2018;8(8):7113. https://doi.org/10.1021/acscatal.8b01014.

[99] Qiu Y, Peng X, Lü F, Mi Y, Zhuo L, Ren J, Liu X. Luo J. Single-atom catalysts for the electrocatalytic reduction of nitrogen to ammonia under ambient conditions. Chem Asian J. 2019: 14(17). https://doi.org/10.1002/asia.201900793.

[100] Guo X, Huang S. Tuning nitrogen reduction reaction activity via controllable Fe magnetic moment: a computational study of single Fe atom supported on defective graphene. Electrochim Acta. 2018;284:392. https://doi.org/10.1016/j.electacta.2018.07.168.

[101] Zhang Q. Guan J. Single-atom catalysts for electrocatalytic applications. Adv Funnct Mater. 2020;30(31):2000768. https://doi.org/10.1002/adfm.202000768.

[102] Li L, Chang X, Lin X, Zhao ZJ, Gong J. Theoretical insights into single-atom catalysts. Chem Soc Rev. 2020;49(22):8156. https://doi.org/10.1039/D0CS00795A.

[103] Huang J, Zhang Q, Ding J, Zhai Y. Fe-N-C single atom catalysts for the electrochemical conversion of carbon, nitrogen and oxygen elements. Mater Rep Energy. 2020;2(3):100141. https://doi.org/10.1016/j.matre.2022.100141.

[104] Wang Y, Wang D, Li Y. rational design of single-atom site electrocatalysts: from theoretical understandings to practical applications. Adv Mater. 2021;33(34):2008151. https://doi.org/10.1002/adma.202008151.

[105] Zhang S, Jin M, Shi T, Han M, Sun Q, Lin Y, Ding Z, Zheng LR, Wang G. Zhang Y. Electrocatalytically active Fe-(O-C_2)$_4$ single-atom sites for efficient reduction of nitrogen to ammonia. Angew Chem. 2020;132(32):13525. https://doi.org/10.1002/anie.202005930.

[106] Su H, Chen L, Chen Y, Si R, Wu Y, Wu X, Geng Z, Zhang W, Zeng J. Single atoms of iron on MoS_2 nanosheets for N_2 electroreduction into ammonia. Angew Chem. 2020;132(46):20591. https://doi.org/10.1002/anie.202009217.

[107] Li J, Chen S, Quan F, Zhan G, Jia F, Ai Z, Zhang L. Accelerated dinitrogen electroreduction to ammonia via interfacial polarization triggered by single-atom protrusions. Chem. 2020;6(4):885. https://doi.org/10.1016/j.chempr.2020.01.013.

[108] Mukherjee S, Yang X, Shan W, Samarakoon W, Karakalos S, Cullen DA, More K, Wang M, Feng Z, Wang G. Atomically dispersed single Ni site catalysts for nitrogen reduction toward electrochemical ammonia synthesis using N_2 and H_2O. Small Methods. 2020;4(6):1900821. https://doi.org/10.1002/smtd.201900821.

[109] Guo X, Wan X, Shui J. Molybdenum-based materials for electrocatalytic nitrogen reduction reaction. Cell Rep Phys Sci. 2021;2(6):100447. https://doi.org/10.1016/j.xcrp.2021.100447.

[110] Zhang C, Wang Z, Lei J, Ma L, Yakobson BI, Tour JM. Atomic molybdenum for synthesis of ammonia with 50% Faradic efficiency. Small. 2022;18(15):2106327. https://doi.org/10.1002/smll.202106327.

[111] Hui L, Xue Y, Yu H, Liu Y, Fang Y, Xing C, Huang B, Li Y. Highly efficient and selective generation of ammonia and hydrogen on a graphdiyne-based catalyst. J Am Chem Soc. 2019;141(27):10677. https://doi.org/10.1021/jacs.9b03004.

[112] Ma Y, Yang T, Zou H, Zang W, Kou Z, Mao L, Feng Y, Shen L. Synergizing Mo single atoms and Mo_2C nanoparticles on CNTs synchronizes selectivity and activity of electrocatalytic N_2 reduction to ammonia. Adv Mater. 2020;32(33):2002177. https://doi.org/10.1002/adma.202002177.

[113] Wang X, Wu D, Liu S, Zhang J, Fu X-Z, Luo J-L. Folic acid self-assembly enabling manganese single-atom electrocatalyst for selective nitrogen reduction to ammonia. Nano Micro Lett. 2021;13(1). https://doi.org/10.1007/s40820-021-00651-1.

[114] Wei ZX, Zhu YT, Liu JY, Zhang ZC, Hu WP, Xu H, Ma JM. Recent advance in single-atom catalysis. Rare Metals. 2021;40(4):767. https://doi.org/10.1007/s12598-020-01592-1.

[115] Wen Y, Zhu H, Hao J, Lu S, Zong W, Lai F, Ma P, Dong W, Liu T, Du M. Metal-free boron and sulphur Co-doped carbon nanofibers with optimized p-band centers for highly efficient nitrogen electroreduction to ammonia. Appl Catal B Environ. 2021;292:120144. https://doi.org/10.1016/j.apcatb.2021.120144.

[116] Yu X, Han P, Wei Z, Huang L, Gu Z, Peng S, Ma J, Zheng G. Boron-doped graphene for electrocatalytic N_2 reduction. Joule. 2018;2(8):1610. https://doi.org/10.1016/j.joule.2018.06.007.

[117] Liu C, Li Q, Wu C, Zhang J, Jin Y, MacFarlane DR, Sun C. Single-boron catalysts for nitrogen reduction reaction. J Am Chem Soc. 2019;141(7):2884. https://doi.org/10.1021/jacs.8b13165.

[118] Chen H, Liang X, Liu Y, Ai X, Asefa T, Zou X. Active site engineering in porous electrocatalysts. Adv Mater. 2020;32(44):2002435. https://doi.org/10.1002/adma.202002435.

[119] Yao Y, Zhu S, Wang H, Li H, Shao MA. Spectroscopic study on the nitrogen electrochemical reduction reaction on gold and platinum surfaces. J Am Chem Soc. 2018;140(4):1496. https://doi.org/10.1021/jacs.7b12101.

[120] Yin H, Li SL, Gan LY, Wang P. Pt-embedded in monolayer g-C_3N_4 as a promising single-atom electrocatalyst for ammonia synthesis. J Mater Chem. A. 2019;7(19):11908. https://doi.org/10.1039/C9TA01624D.

[121] Saeidi N, Esrafili MD, Sardroodi JJ. Electrochemical reduction of N_2 to NH_3 using a Co-atom stabilized on defective N-doped graphene: a computational study. Chem Select. 2019;4(42):12216. https://doi.org/10.1002/slct.201903206.

[122] Huang Y, Yang T, Yang L, Liu R, Zhang G, Jiang J, Luo Y, Lian P, Tang S. Graphene–boron nitride hybrid-supported single Mo atom electrocatalysts for efficient nitrogen reduction reaction. J Mater Chem. A. 2019;7(25):15173. https://doi.org/10.1039/C9TA02947H.

[123] Ling C, Ouyang Y, Li Q, Bai X, Mao X, Du A, Wang J. A General two-step strategy-based high-throughput screening of single atom catalysts for nitrogen fixation. Small Methods. 2018;3(9):1800376. https://doi.org/10.1002/smtd.201800376.

[124] He T, Matta SK, Du A. Single tungsten atom supported on N-doped graphyne as a high-performance electrocatalyst for nitrogen fixation under ambient conditions. Phys Chem. 2019;21(3):1546. https://doi.org/10.1039/C8CP06978F.

[125] Bian X, Zhao Y, Zhang S, Li D, Shi R, Zhou C, Zhang, T. Enhancing the supply of activated hydrogen to promote photocatalytic nitrogen fixation. ACS Mater Lett. 2021;3(11):1521. https://doi.org/10.1021/acsmaterialslett.1c00504.

[126] Huang H, Shi R, Zhang X, Zhao J, Su C, Zhang T. Photothermal-assisted triphase photocatalysis over a multifunctional bilayer paper. Angew Chem Int Ed. 2021;60(42):22963. https://doi.org/10.1002/anie.202110336.

[127] Zhou P, Chao Y, Lv F, Lai J, Wang K, Guo S. Designing noble metal single-atom-loaded two-dimension photocatalyst for N_2 and CO_2 reduction via anion vacancy engineering. Sci Bull. 2020;65(9):720−725. https://doi.org/10.1016/j.scib.2019.12.025.

[128] Zhao Z, Park J, Choi C, Hong S, Hui X, Zhang H, Lo TWB, Robertson AW, Lv Z, Jung Y, Sun Z. Engineering vacancy and hydrophobicity of two-dimensional $TaTe_2$ for efficient and stable

electrocatalytic N_2 reduction. The Innovation. 2022;3(1):100190. https://doi.org/10.1016/j.xinn.2021.100190.

[129] Li Y, Zhang Q, Li C, Fan HN, Luo WB, Liu HK, Dou SX. Atomically dispersed metal dimer species with selective catalytic activity for nitrogen electrochemical reduction. J Mater Chem A. 2019;7(39):22242. https://doi.org/10.1039/C9TA07845B.

[130] Xi J, Jung HS, Xu Y, Xiao F, Bae JW, Wang, S. Synthesis strategies, catalytic applications, and performance regulation of single-atom catalysts. Adv Func Mater. 2021;31(12):2008318. https://doi.org/10.1002/adfm.202008318.

[131] Cheng H, Ding LX, Chen GF, Zhang L, Xue J, Wang H. Molybdenum carbide nanodots enable efficient electrocatalytic nitrogen fixation under ambient conditions. Adv Mater. 2018;30(46):1803694. https://doi.org/10.1002/adma.201803694.

[132] Chen ZW, Yan JM, Jiang Q. Single or double: which is the altar of atomic catalysts for nitrogen reduction reaction? Small Methods. 2019;3(6):1800291. https://doi.org/10.1002/smtd.201800291.

[133] Qiu N, Li J, Wang H, Zhang Z. Emerging dual-atomic-site catalysts (DASCs) for electrocatalytic CO_2 reduction. Sci China Mater. 2022. https://doi.org/10.1007/s40843-022-2189-x.

[134] Yang C, Zhu Y, Liu J, Qin Y, Wang H, Liu H, Hu W. Defect engineering for electrochemical nitrogen reduction reaction to ammonia. Nano Energy. 2020;77:105126. https://doi.org/10.1016/j.nanoen.2020.105126.

[135] Chen C, Sun M, Wang K, Li Y. Dual-metal single-atomic catalyst: the challenge in synthesis, characterization, and mechanistic investigation for electrocatalysis. SmartMat. 2022. https://doi.org/10.1002/smm2.1085.

Biographical sketch

Zhenyu Sun completed his PhD at the Institute of Chemistry Chinese Academy of Sciences. He carried out postdoctoral research at Trinity College Dublin, Ruhr University Bochum, and the University of Oxford. He is currently a full professor at the College of Chemical Engineering at Beijing University of Chemical Technology (China). He was awarded a Humboldt Research Fellowship for Experienced Researchers (Germany) in 2012. His current research mainly focuses electrocatalytic N_2/CO_2 reduction reactions.